

Metallicity of the intermediate velocity H I clouds derived based on the sub-mm dust emission for the whole sky

Takahiro Hayakawa,¹* and Yasuo Fukui¹

¹*Department of Physics, Nagoya University, Furo-cho Chikusa-ku, Nagoya 464-8602, Japan*

Accepted XXX. Received YYY; in original form ZZZ

ABSTRACT

We have carried out a multiple regression analysis of the 21 cm H I emission combined with the sub-mm dust emission over 80 per cent of the sky at a resolution of 47 arcmin. The method covers the sky contiguously, and is distinguished from the optical absorption line measurements toward bright stars which cover a tiny fraction of the gas. On the assumption that the dust-to-gas ratio is proportional to the metallicity, we derived the metallicity of all the H I components, i.e., the intermediate velocity clouds (IVCs), the high velocity clouds (HVCs), as well as the local H I gas. Major results include that the metallicity of the IVCs is in a range of 0.1 – 1.5 (relative to the majority of local diffuse H I gas) with a mode at 0.6, and that a significant fraction, ~ 30 per cent, of the IVCs includes the low metallicity gas of < 0.3. In addition, it is revealed that 80 per cent of the HVC Complex C has a metallicity of < 0.3, and that the Magellanic Stream has a uniform very low metallicity of < 0.1. We argue that a large fraction of the low metallicity IVC gas may favor a picture of the external low-metallicity H I gas accretion instead of the Galactic-fountain model. In addition, we find that the IVCs show a trend that metallicity of the IVCs increases with velocity decrease, suggesting that the IVCs are accumulating high metallicity halo gas via dynamical interaction at $z < 1$ kpc.

Key words: ISM: abundance – ISM: atoms – ISM: clouds — Galaxy: halo

1 INTRODUCTION

The intermediate velocity clouds (IVCs) in a velocity range of 40 – 100 km s⁻¹ are not explained by a simple model of the galactic rotation, but are not so extreme as the high velocity clouds (HVCs) whose velocity is higher than 100 km s⁻¹. The IVCs have been discovered predominantly in a negative radial velocity range, as well as the HVCs, through absorption line observations (e.g., Adams 1949; Munch 1952; Münch & Zirin 1961) and H I 21 cm line surveys (e.g., Blaauw & Tolbert 1966; Wesselius & Fejes 1973). There have been several efforts to constrain the distance to the IVCs/HVCs using the absorption-line bracketing technique. The IVCs are located relatively close, have typical z heights of ~ 1 – 2 kpc (e.g., Wakker et al. 2008; Lehner et al. 2022, see also compilations by Wakker 2001; van Woerden & Wakker 2004 and references therein), and are likely to be the disk-halo interface objects, while the major HVCs are further away, several to ~ 10 kpc above the disk (e.g., van Woerden et al. 1999; Thom et al. 2006, 2008; Wakker et al. 2007, 2008; Smoker et al. 2011; Richter et al. 2015; Lehner et al. 2022) and belong to the inner halo. One of the important questions is whether the IVCs and HVCs are different halo-cloud populations (i.e., gas comes from the disk and the one fuels the disk) or just the same population of objects with different heights and radial velocities.

The metallicity is a crucial parameter for pursuing the origin and has traditionally been measured by observing absorption lines. The previous works presented that the HVCs have sub-solar metallicities $Z/Z_{\odot} \lesssim 0.1$ (e.g., Schwarz et al. 1995; Wakker et al. 1999; Richter

et al. 2001b; Tripp et al. 2003; Collins et al. 2003; Sembach et al. 2004) and are of extra-galactic origin. The IVCs have near-solar metallicity of ~ 0.5 – 1.0 solar (Wakker 2001 and references therein, Richter et al. 2001a,b) and are usually explained by the so-called Galactic-fountain model in which hot gas ejected from the disk by the stellar feedback falls back in the form of neutral clouds (Shapiro & Field 1976; Bregman 1980). However, the measured metallicities often have rather large uncertainties due to such factors as ionization states and the interstellar depletion (van Woerden & Wakker 2004 summarized the possible problems in the metallicity determination, see section 5 of the reference). For instance, Hernandez et al. (2013) claimed that IVC 135+54–45 (cataloged as IV 21 in Kuntz & Danly 1996) has a sub-solar metallicity of $\log(Z/Z_{\odot}) = -0.43 \pm 0.12$ dex ($Z/Z_{\odot} = 0.37 \pm 0.12$), but this is incompatible with the bright FIR emission suggesting the existence of a large amount of dust¹. In addition, these measurements are made at a limited number of locations because of a tiny number of bright background stars and do not lead to firmly establish the metallicity of the IVC.

An alternative method to measure the metallicity, the dust emission such as the 100 μ m emission obtained with *IRAS* is a reasonable proxy of the metal abundance since the dust consists of a significant

¹ Hernandez et al. (2013) also claimed that the dust-to-gas (100 μ m intensity to H I column density) ratio of IVC 135+54–45, 0.32×10^{-20} (MJy sr⁻¹ cm²), is one-third of the usual solar-neighborhood ratio. However, Weiß et al. (1999) found ~ 1×10^{-20} (MJy sr⁻¹ cm²) and Lenz et al. (2015) 0.7–1.2 $\times 10^{-20}$ (MJy sr⁻¹ cm²) for the IVC. Lenz et al. (2015) surmised that this is because Hernandez et al. (2013) used *IRAS* data instead of the reprocessed IRIS data.

* E-mail: t.hayakawa@phys.nagoya-u.ac.jp (TH)

fraction of heavy elements, which is perhaps comparable to that in the gas phase, as indicated by the uniform dust-to-gas mass ratio of 1/100 in the interstellar medium (ISM). However, the $100\ \mu\text{m}$ dust emission is not proportional to the dust mass. This non-linearity, which hampered to use the dust emission for quantification of the metallicity, is eliminated at sub-mm wavelengths, where the modified Planck function is linearized completely in the Rayleigh-Jeans regime. Therefore, the sub-mm dust emission is well proportional to the total dust mass. The Planck Collaboration obtained such sensitive sub-mm dust emission over the whole sky at a 5 arcmin resolution and derived dust optical depth at 353 GHz ($850\ \mu\text{m}$), τ_{353} , by fitting the modified Planck function at four wavelengths from 100 to $850\ \mu\text{m}$ obtained by *Planck* and *IRAS* (Planck Collaboration XI 2014; Planck Collaboration Int. XLVIII 2016).

Previous works by Fukui et al. (2014, 2015), Okamoto et al. (2017, O17 hereafter), Hayashi et al. (2019a, H19), and Hayashi et al. (2019b) showed that τ_{353} characterizes well the linearity of the dust emission in a number of regions of the Milky Way. The scheme was also applied to the Large Magellanic Cloud (LMC). As such, Fukui et al. (2017) used the linear relationship between the velocity-integrated intensity of H I line, $W_{\text{H I}}$, and τ_{353} , and estimated that the H I ridge including R136 has a factor of two lower metallicity (dust-to-gas ratio) than the optical stellar Bar region in LMC. In addition, Tsuge et al. (2019) presented that the N44 region near the H I Ridge in the LMC have a ~ 30 per cent lower metallicity than that of the Bar region. Most recently, Fukui et al. (2021, F21 hereafter) applied the method to IVC 86–36 in the Pegasus-Pisces (PP) Arch and derived the upper limit of the dust-to-H I ratio of IVC 86–36 to be less than ~ 0.2 of the local ISM, strongly suggesting that PP Arch originated in a low-metallicity environment but not in the disk. Their measurements of the dust-to-gas ratio significantly improved the preceding metallicity measurements by optical/ultraviolet atomic absorption lines of the background stellar spectrum in the IVC (Fitzpatrick & Spitzer 1997). Although the absorption-line results suggest the subsolar metal abundance, the abundance values vary by ~ 0.5 dex depending on the atomic species, leaving the metallicity unquantified.

Considering the whole above, we judge the dust-to-gas ratio measurements (Fukui et al. 2017; Tsuge et al. 2019 and F21) to be most appropriate and adopt it in the present work with an aim to extend the metallicity measurement of the H I gas over the whole sky outside the Galactic plane. A new feature in the present work is to employ a multiple-regression technique to analyze the relationship between $W_{\text{H I}}$ of multiple velocity components and the total amount of τ_{353} . Another is the geographically weighted regression (GWR) technique (Brunsdon et al. 1996; Fotheringham et al. 2002) which allows us to derive the spatial distribution of the dust-to-gas ratio.

The paper is organized as follows; Section 2 describes the datasets used, and Section 3 gives the dust and gas properties analyzed by the present work. Section 4 shows the dust-to-gas ratio distribution of the H I components such as the IVCs and HVCs, and the metallicity distribution in the whole sky including the individual outstanding components. Section 5 gives a discussion focusing on the implications of the IVC metallicity. Section 6 concludes the present work.

2 DATASETS

2.1 H I data

Archival data of HI4PI full-sky survey (HI4PI Collaboration 2016) were used in the present study. HI4PI combined the data from the

first release of the Effelsberg-Bonn H I Survey (EBHIS, Winkel et al. 2016) and the third revision of the Galactic All-Sky Survey (GASS, Kalberla & Haud 2015). The data were divided into 192 parts, and each of them was presented as a FITS binary table containing spectra on the HEALPIX² grid with a resolution parameter of $N_{\text{side}} = 1024$ (the mean pixel spacing is 3.4 arcmin). The brightness temperature noise level is ~ 43 mK (rms) at a velocity resolution of $1.49\ \text{km s}^{-1}$. The velocity coverage (with respect to the Local Standard of Rest, LSR) is $|V_{\text{LSR}}| \leq 600\ \text{km s}^{-1}$ (EBHIS part) or $|V_{\text{LSR}}| \leq 470\ \text{km s}^{-1}$ (GASS part). The FWHM angular resolution of the combined map is 16.2 arcmin, twice better than the Leiden/Argentine/Bonn (LAB) Survey (Kalberla et al. 2005).

The H I data were integrated into the five velocity ranges listed in Table 1 and combined into a single HEALPIX format data for each velocity range.

2.2 Dust optical depth data

Planck Collaboration Int. XLVIII (2016) used *Planck* 2015 data release (PR2) maps and separated Galactic thermal dust emission from cosmic infrared background anisotropies by implementing the generalized needlet internal linear combination (GNILC) method. The GNILC dust maps have a variable angular resolution with an effective beam FWHM varying from 5 to 21.8 arcmin (see Planck Collaboration Int. XLVIII 2016, figure 2). The authors then produced the dust optical depth, temperature, and spectral index maps by fitting a modified blackbody model to the GNILC dust maps at 353, 545, 857 GHz, and *IRAS* $100\ \mu\text{m}$ map. We used the τ_{353} data released version R2.01 in HEALPIX format with $N_{\text{side}} = 2048$ (the mean pixel spacing is 1.7 arcmin). The median relative uncertainty in τ_{353} is $\sigma(\tau_{353})/\tau_{353} = 0.037$ in $|b| > 15^\circ$.

2.3 CO data

We used the *Planck* PR2 type 2 CO(1–0) map (Planck Collaboration X 2016) to trace the distribution of molecular gas. The type 2 map was obtained by combining the *Planck* 100, 143, and 353 GHz channel maps to extract the CO(1–0) line and has a higher signal-to-noise ratio than the type 1 map which is based on a single channel approach. The angular resolution is 15 arcmin FWHM. The median uncertainty in the CO integrated intensity is $\sigma(W_{\text{CO}}) = 0.44\ \text{K km s}^{-1}$ in $|b| > 15^\circ$.

2.4 H α data

We used Wisconsin H α Mapper Sky Survey (WHAM-SS) DR1-v161116-170912 which combines the Northern Sky Survey (NSS) in $\delta \gtrsim -30^\circ$ (Haffner et al. 2003) and the Southern Sky Survey (SSS) data (Haffner et al. 2010) ($\delta \lesssim -30^\circ$). The WHAM-SS is the sole velocity-resolved all-sky H α survey publicly available at present, covering velocity ranges roughly from $V_{\text{LSR}} = -100$ to $+100\ \text{km s}^{-1}$ with a $12\ \text{km s}^{-1}$ resolution.

2.5 Pre-processing of the data

The HI4PI H I data and *Planck* dust data have different resolutions. We processed the data as follows; (1) If the τ_{353} data have a 21.8 arcmin resolution at a data point, the H I data were smoothed. Otherwise, the dust data were smoothed to 16.2 arcmin resolution.

² <http://healpix.sourceforge.net/>

(2) Both were degraded to $N_{\text{side}} = 256$ (the mean pixel spacing is 13.7 arcmin). In the following sections, we used these processed data unless otherwise noted.

3 GAS AND DUST PROPERTIES

3.1 Neutral gas and dust optical depth

Fig. 1 shows the spatial distributions of $W_{\text{H I}}$ in the negative (i.e., blue-shifted) intermediate velocity (NIV, $V_{\text{LSR}} = -100 - -30 \text{ km s}^{-1}$), positive (red-shifted) intermediate velocity (PIV, $V_{\text{LSR}} = +30 - +100 \text{ km s}^{-1}$), and low velocity (LV, $|V_{\text{LSR}}| < 30 \text{ km s}^{-1}$) components, respectively. Those of the negative- and positive high-velocity (NHV and PHV, $|V_{\text{LSR}}| > 100 \text{ km s}^{-1}$) components are also shown as silhouettes. Fig. 2 shows the distribution function of the apparent amount of H I gas (the product of $W_{\text{H I}}$ and the solid angle s) as a function of the column density

$$N_{\text{H I}}^* = C_0 W_{\text{H I}} = 1.82 \times 10^{18} (\text{cm}^{-2} \text{K}^{-1} \text{km}^{-1} \text{s}) W_{\text{H I}} \quad (1)$$

in the five velocity ranges (the asterisk means the H I column density is under the optically-thin approximation ($\tau_{\text{H I}} \ll 1$), following the notation of Fukui et al. 2014, 2015, O17 and H19). As reported in the previous works, the IVCs are mainly in the negative velocity ranges. The NIV components are concentrated in giant IVC complexes IV Arch, IV Spur, and Low-Latitude (LL) IV Arch, occupying one-third of $b > 15^\circ$ skies. Another conspicuous IVC, PP Arch, is located in the Galactic South and has a head-tail structure elongated from IVC 86–36 to $(l, b) = (150^\circ, -60^\circ)$. The only small apparent amount of H I gas is in the positive velocity ranges, except for the Magellanic System. The LV components covering the whole sky are considered to be the local volume gas within 300 pc of the sun. They have an H I column density range of $10^{20} - 10^{21} \text{ cm}^{-2}$ with a peak at $3 - 4 \times 10^{20} \text{ cm}^{-2}$, which is one order of magnitude higher than IVCs (1×10^{19} to $2 \times 10^{20} \text{ cm}^{-2}$) and HVCs ($\lesssim 1 \times 10^{20} \text{ cm}^{-2}$).

Fig. 3 shows the spatial distribution of τ_{353} , and Fig. 4 shows the correlation plots between τ_{353} and $W_{\text{H I}}$ in the $|b| > 15^\circ$ skies with masking described in Appendix A. The τ_{353} values are the total amount on the line-of-sights, but the $W_{\text{H I}}$ values are obtained by integrating within each velocity range. The good correlation between the two quantities is found only in the LV component, while the other H I gas components show a rather poor correlation between them. The plots demonstrate that the gas in the intermediate- and high-velocity components has significantly different properties showing little correlation with τ_{353} . A trend that is seen in high- to intermediate-velocity components is the vertical features at $\tau_{353} \sim 1 \times 10^{-6}$ in Fig. 4, which indicate little dependence of $W_{\text{H I}}$ on τ_{353} . We suggest these vertical features, although not dominant, indicate low metallicity gas included in the high- to intermediate-velocity components as described later in Section 5. For the rest of the points scattered broadly, τ_{353} shows no correlation with the IVCs or the HVCs.

3.2 Contribution of the Ionized Gas to the Dust Optical Depth

The diffuse warm ionized medium (WIM) outside of localized H II regions is another significant component of the ISM. The diffuse WIM distributed in the thick disk is estimated to have a surface density of approximately one-third of H I (Reynolds 1991). The absorption-line studies revealed that HVCs and IVCs are associated with the ionized components (e.g., Sembach et al. 2003; Shull et al. 2009; Lehner & Howk 2011). The velocity-resolved high-sensitivity surveys of diffuse H α emission using WHAM showed that the neutral and ionized

components trace each other well, though the detailed structure is not identical (e.g., Tufte et al. 1998; Haffner et al. 2001; Barger et al. 2012). The estimated mass of the associated ionized component is comparable to that of the neutral counterpart.

Previous works reported the observational evidence for the dust in the WIM (Howk & Savage 1999; Dobler et al. 2009). However, the dust properties in the diffuse WIM are still not well understood. The destruction of the dust grains is expected in the low-density ISM (e.g., McKee 1989) and the WIM could be dust poor by grain-grain sputtering, in particular, in the H/IVCs which are colliding with the halo warm gas at supersonic velocity of $30 - 200 \text{ km s}^{-1}$ (e.g., Jones et al. 1994).

In order to approximately and empirically quantify the dust emission related to the WIM, we examined the relationship between $N_{\text{H I}}^*$, N_{H^+} , and τ_{353} . The column density of the ionized hydrogen N_{H^+} is converted from H α intensity ($I_{\text{H}\alpha}$) by a conversion factor $N_{\text{H}^+} = 3 \times 10^{20} (\text{cm}^{-2} \text{R}^{-1}) I_{\text{H}\alpha}$ (see Appendix B), where $1 \text{ R} = 10^6/4\pi \text{ photons cm}^{-2} \text{ s}^{-1} \text{ sr}^{-1}$. Fig. 5, the distribution of $I_{\text{H}\alpha}$ in the NIV, LV, and PIV velocity ranges, shows that the WHAM-SSS (Haffner et al. 2010) data in $\delta \lesssim -30^\circ$ suffer from block discontinuity (0.2 R rms, corresponding to $6 \times 10^{19} \text{ cm}^{-2}$ using the conversion factor above) probably due to some data-reduction issue. We thus made the regression analysis in the two regions in the NSS part ($\delta > -30^\circ$) shown in Fig. 5. The region (1) is the main part of IV Arch and Spur ($l = 90^\circ - 270^\circ, b > 60^\circ$), and the region (2) is in the middle-to-high latitude ($l < 30^\circ$ or $l > 330^\circ, b > 30^\circ$). Both regions were set by avoiding the HVCs and strong compact H α sources. The WHAM survey is undersampled with a 1 deg beam at a 1 deg spacing (see Haffner et al. 2003, section 2.2), having a $\sim 3 - 12$ times lower resolution than the HI4PI and Planck data, and we convolved the $N_{\text{H I}}^*$ and τ_{353} data with the WHAM beam centered on each WHAM pointing. Following Finkbeiner (2003), we approximated the WHAM beam to be a smoothed top-hat function

$$f(\theta) = \frac{1}{\exp[(\theta - \theta_0)/\theta_s] + 1}, \quad (2)$$

where θ is the angular distance from the beam center, θ_0 and θ_s are set to 0.5 and 0.025 deg, respectively.

Fig. 6 shows the τ_{353} - $N_{\text{H I}}^*$ and τ_{353} - N_{H^+} correlations in the NIV, LV and PIV velocity ranges. It is shown that τ_{353} does not show any sign of dependence on N_{H^+} , while τ_{353} is clearly correlated with $N_{\text{H I}}^*$. We therefore confirm that the dust emission from the ionized component is not significantly contributing to τ_{353} and can be ignored in the present analysis. Note that Lagache et al. (2000) previously concluded that the dust emissivity ($\tau_\lambda/N_{\text{H}^+}$ at a wavelength λ) in the WIM is close to the one in the H I. However, the authors used four times smaller $N_{\text{H}^+}/I_{\text{H}\alpha}$ conversion factor than the one in the present study, which overestimates the dust emissivity and is unacceptable.

4 THE ESTIMATE OF THE DUST-TO-GAS RATIO

4.1 Formulation

The observed τ_{353} is the sum of the contribution of each component,

$$\tau_{353} = \sum_X (\tau_{353,X,\text{H}^+} + \tau_{353,X,\text{H I}} + \tau_{353,X,\text{H}_2}), \quad (3)$$

where $X = \text{NHV, NIV, } \dots, \text{ PHV}$ represents the velocity ranges listed in Table 1, τ_{353,X,H^+} , $\tau_{353,X,\text{H I}}$, and τ_{353,X,H_2} are the contribution of ionized, atomic, and molecular gas in the velocity

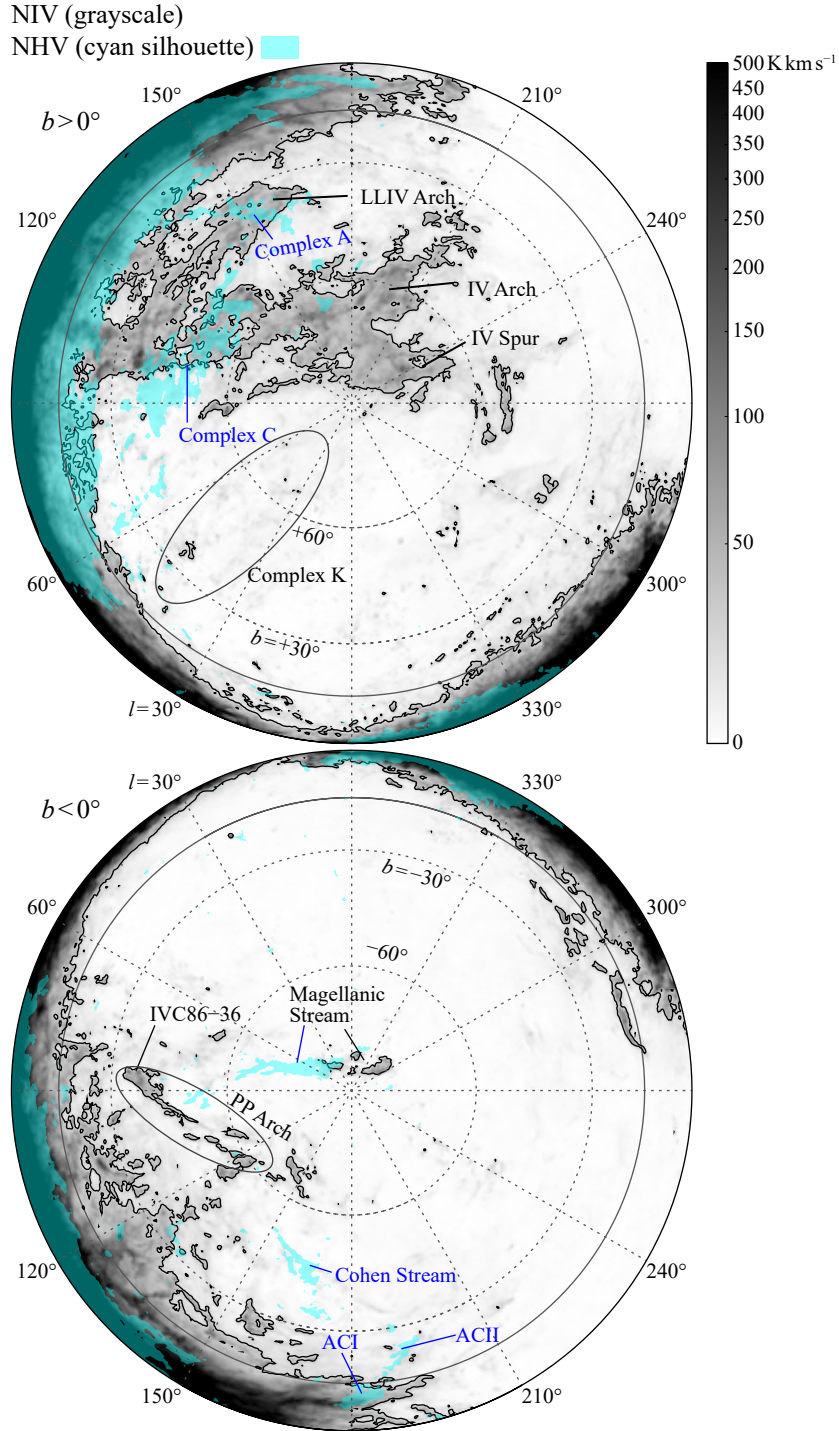


Figure 1. (a) The grayscale image shows the spatial distribution of H I integrated intensity in the NIV velocity range ($V_{\text{LSR}} = -100 - -30 \text{ km s}^{-1}$, see Table 1), $W_{\text{H I, NIV}}$, in a zenithal equal area (ZEA) projection (HI4PI Collaboration 2016). The contours show $W_{\text{H I, NIV}} = 30 \text{ K km s}^{-1}$. The overlaid cyan silhouette shows the NHV components ($V_{\text{LSR}} = -470 - -100 \text{ km s}^{-1}$) with $W_{\text{H I, NHV}} > 10 \text{ K km s}^{-1}$. Upper panels cover $b > 0^\circ$ and longitude increases clockwise. Lower panels cover $b < 0^\circ$ and longitude increases counter clockwise. Both join at $(l, b) = (0^\circ, 0^\circ)$. The gray solid lines indicate $|b| = 15^\circ$.

range X , respectively. We masked the regions where CO integrated-intensity $W_{\text{CO}} > 1.4 \text{ K km s}^{-1}$ (corresponding to the 3σ noise level in $|b| > 15^\circ$), and the molecular fraction can be approximated to be zero in the unmasked regions. If we assume that the contribution of the ionized gas is negligibly small (see Section 3.2), then equation (3)

can be rewritten as

$$\tau_{353} = \sum_X \tau_{353, X, \text{H I}}. \quad (4)$$

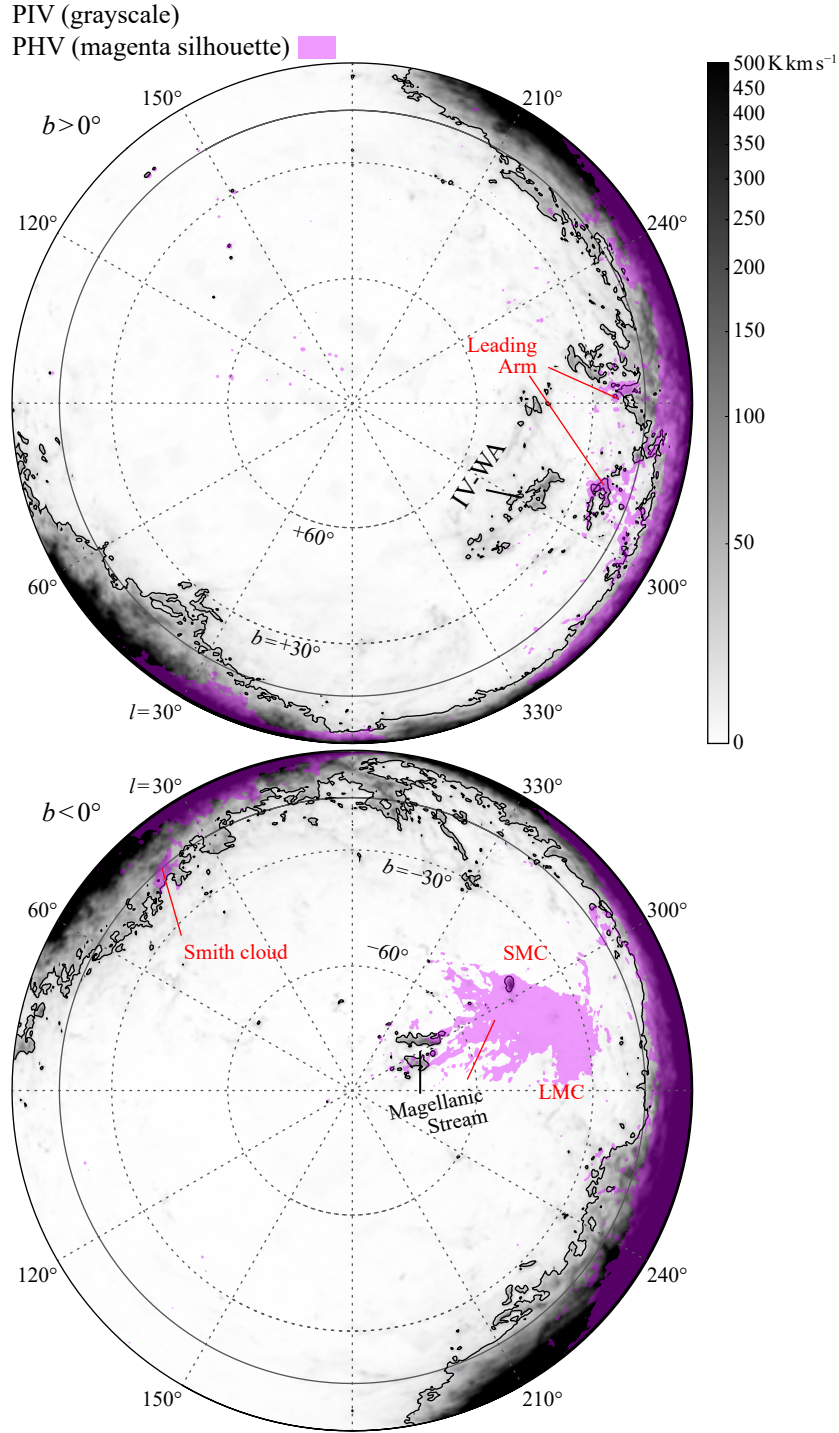


Figure 1 – continued (b) The grayscale image shows the PIV components ($V_{\text{LSR}} = +30 - +100 \text{ km s}^{-1}$) and the contours show $W_{\text{H I,PIV}} = 30 \text{ K km s}^{-1}$. The overlaid magenta silhouette shows the PHV components ($V_{\text{LSR}} = +100 - +470 \text{ km s}^{-1}$) with $W_{\text{H I,PHV}} > 10 \text{ K km s}^{-1}$.

The contribution of the velocity component X is expressed as a function of H I column-density $N_{\text{H I},X}$,

$$\tau_{353,X,\text{H I}} = \left(\zeta_X \frac{N_{\text{H I},X}}{C} \right)^\alpha, \quad (5)$$

where ζ_X is the ‘metallicity’ term, or normalized dust-to-gas ratio (that of the reference local ISM is assumed to be 1.0), and C is an empirical constant determined independently. Here, we adopt the

$N_{\text{H I}}$ model having a nonlinear relationship with τ_{353} derived by O17 and H19. These authors used the 21 cm H I data with τ_{353} following Fukui et al. (2014, 2015) by taking into account the optical depth effect of the 21 cm H I emission. O17 derived a τ_{353} - $N_{\text{H I}}$ relationship with $\alpha = 1.3$ and $C = 9.0 \times 10^{24} \text{ cm}^{-2}$ for the H I gas in the Perseus region, and H19 obtained $\alpha = 1.2$ and $C = 2.0 \times 10^{25} \text{ cm}^{-2}$ in the Chamaeleon molecular cloud complex. The value of α greater than 1.0 was suggested to be due to the dust

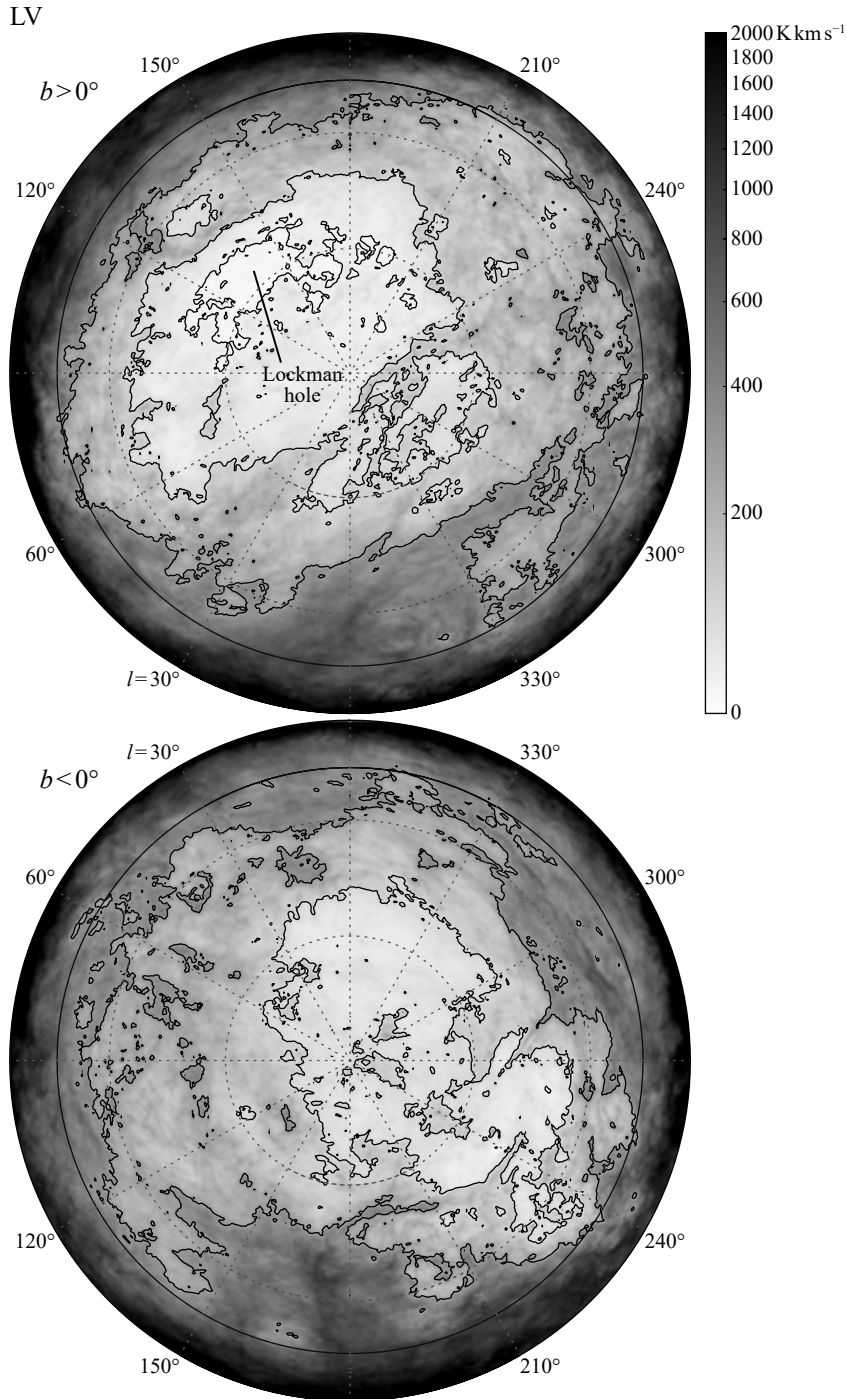


Figure 1 – continued (c) The grayscale image shows the LV components ($V_{\text{LSR}} = -30 - +30 \text{ km s}^{-1}$) and the contours show $W_{\text{H I, LV}} = 30, 100, \text{ and } 300 \text{ K km s}^{-1}$.

evolution effect by [Roy et al. \(2013\)](#) who derived the non-linearity with $\alpha = 1.3$ from (the far infrared optical depth)-(near infrared color excess) relationship in Orion. The [O17](#) and [H19](#) models give slightly different but almost the same τ_{353} value (the difference in τ_{353} is $\lesssim 1 \times 10^{-7}$ for $N_{\text{H}} < 8 \times 10^{20} \text{ cm}^{-2}$), as shown in Fig. 4. [Hayashi et al. \(2019b\)](#) made a *Fermi*-LAT γ -ray analysis and confirmed the

non-linearity with $\alpha \sim 1.4$. Note that [O17](#) and [H19](#)³ used *Planck* 2013 data release (PR1) dust data released version R1.20 ([Planck Collaboration XI 2014](#)), whereas [Hayashi et al. \(2019b\)](#) and the present study used R2.01 data. We compared the two datasets and found a good consistency between $\tau_{353}(\text{R2.01})$ and $\tau_{353}(\text{R1.20})$ (see Appendix C).

³ The description in Section 2.3 of [H19](#), ‘released version R1.10 are used’, is to be corrected to ‘released version R1.20 are used’.

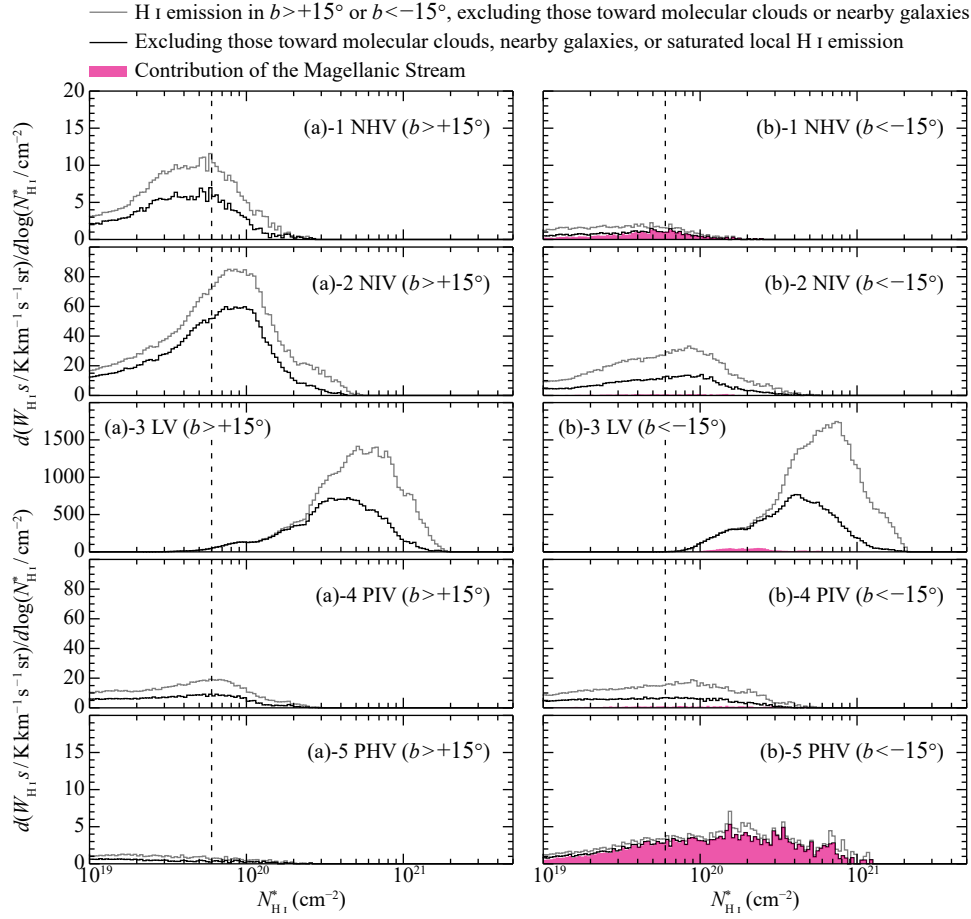


Figure 2. Distribution of the apparent amount of H I gas (the product of $W_{\text{H I}}$ and the solid angle s) as a function of the column density under the optically thin approximation $N_{\text{H I}}^*$ in the NHV, NIV, LV, PIV and PHV velocity ranges (from top to bottom). The panels in the left column are for $b > +15^\circ$, and those in the right column are for $b < -15^\circ$. The gray lines show excluding toward molecular clouds or nearby galaxies (the masking criteria (a) – (c) in Appendix A are applied). The black lines further excluding toward saturated local H I emission (all masking criteria are applied). The shades in magenta show the contribution of the Magellanic Stream. The vertical dashed line in each panel represents a threshold of $N_{\text{H I}}^* = 6 \times 10^{19} \text{ cm}^{-2}$ ($W_{\text{H I}} = 33 \text{ K km s}^{-1}$), beyond which the ‘metallicity’ term (or dust-to-gas ratio) ζ_X in equation (5) can be determined with uncertainties of $\sigma(\zeta_X) \lesssim 0.3$ (see Section 4.2 and Appendix D2).

Table 1. Summary of the velocity ranges in the present study.

Name ^a	V_{LSR} range ^b (km s^{-1})	$M_{\text{H I}} (b > 15^\circ)^c$ (M_\odot)	$M_{\text{H I}} (\text{valid data points})^d$ (M_\odot)	
Negative high velocity (NHV)	−470 – −100	1.9×10^7	1.9×10^6	12%
Negative intermediate velocity (NIV)	−100 – −30	1.5×10^6	4.3×10^5	29%
Low velocity (LV)	−30 – +30	7.0×10^5	3.1×10^5	43%
Positive intermediate velocity (PIV)	+30 – +100	5.3×10^5	7.9×10^4	15%
Positive high velocity (PHV)	+100 – +470	3.7×10^6	2.5×10^5	7%

^a Identification name, and its abbreviation form in parentheses.

^b Minimum and maximum velocities with respect to the LSR.

^c The total H I mass in $|b| > 15^\circ$ skies excluding the Magellanic Stream, obtained by equation (11) assuming distances of 150 pc (LV), 1 kpc (NIV and PIV), and 10 kpc (NHV and PHV).

^d The total H I mass in valid data points and the percentage of whole $M_{\text{H I}}$ in $|b| > 15^\circ$. The valid data points does not meet any of the masking criteria (a) – (d) in Appendix A and have column densities $N_{\text{H I}}^* > 6 \times 10^{19} \text{ cm}^{-2}$ (see Section 4.2).

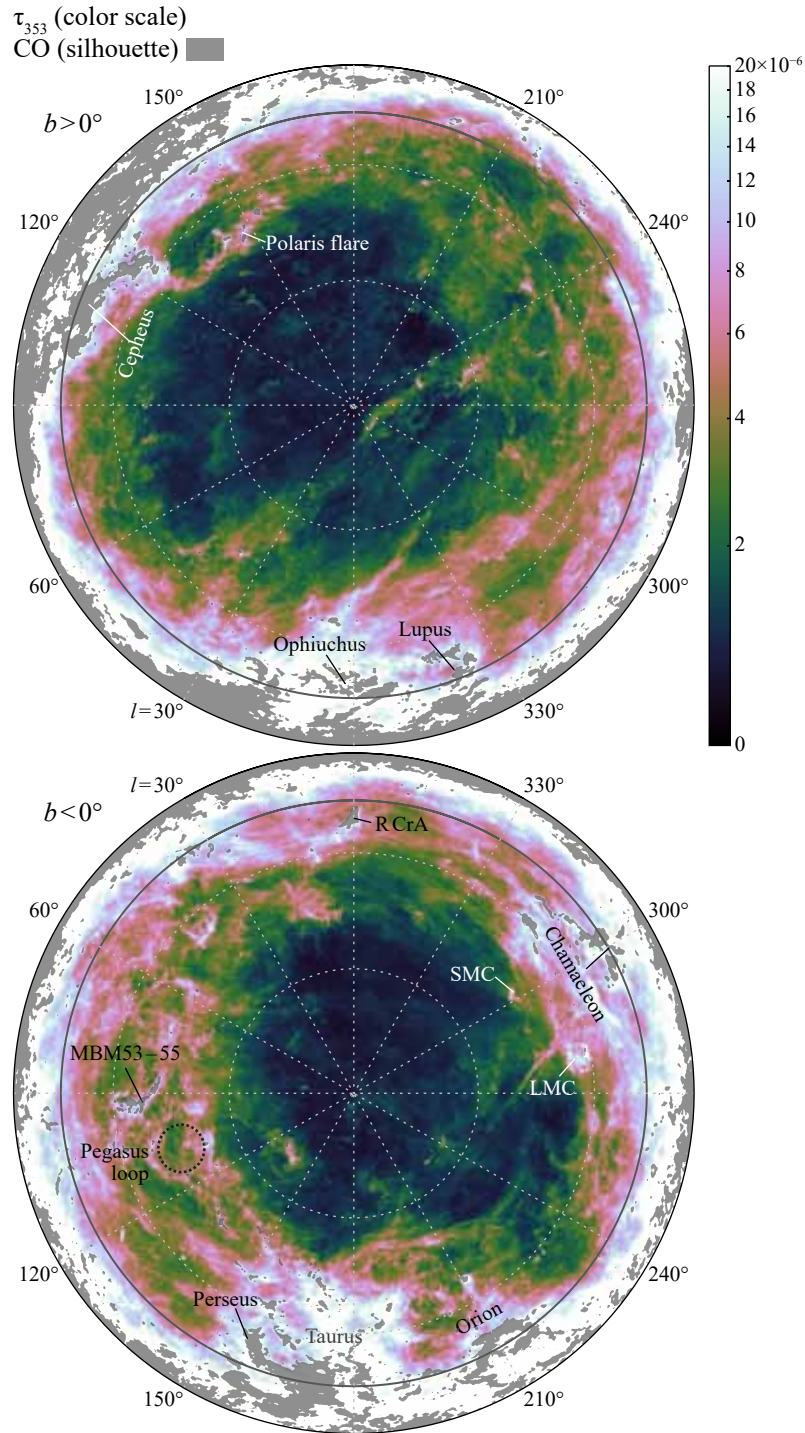


Figure 3. Spatial distribution of 353 GHz dust optical depth (τ_{353}) (Planck Collaboration Int. XLVIII 2016) shown in the same projection as Fig. 1. The overlaid silhouette outlines the molecular clouds with $W_{\text{CO}} > 1.4 \text{ K km s}^{-1}$ (Planck Collaboration X 2016).

The H I column density is expressed as a function of H I integrated intensity $W_{\text{H I}, X}$ and optical depth $\tau_{\text{H I}, X}$,

$$N_{\text{H I}, X} = C_0 \frac{\tau_{\text{H I}, X}}{1 - \exp(-\tau_{\text{H I}, X})} W_{\text{H I}, X}. \quad (6)$$

Suppose that $N_{\text{H I}, X} \sim N_{\text{H I}, X}^* = C_0 W_{\text{H I}, X}$ under the optically thin approximation of the H I emission ($\tau_{\text{H I}, X} \ll 1$), then equations (5)

and (6) give

$$\tau_{353, X, \text{H I}} = \left(\zeta_X \frac{C_0}{C} W_{\text{H I}, X} \right)^\alpha \quad (7)$$

and equation (4) can be rewritten as

$$\tau_{353} = \left(\frac{C_0}{C} \right)^\alpha \sum_X (\zeta_X W_{\text{H I}, X})^\alpha. \quad (8)$$

Equation (8) is reformed by introducing spatially varying coefficients

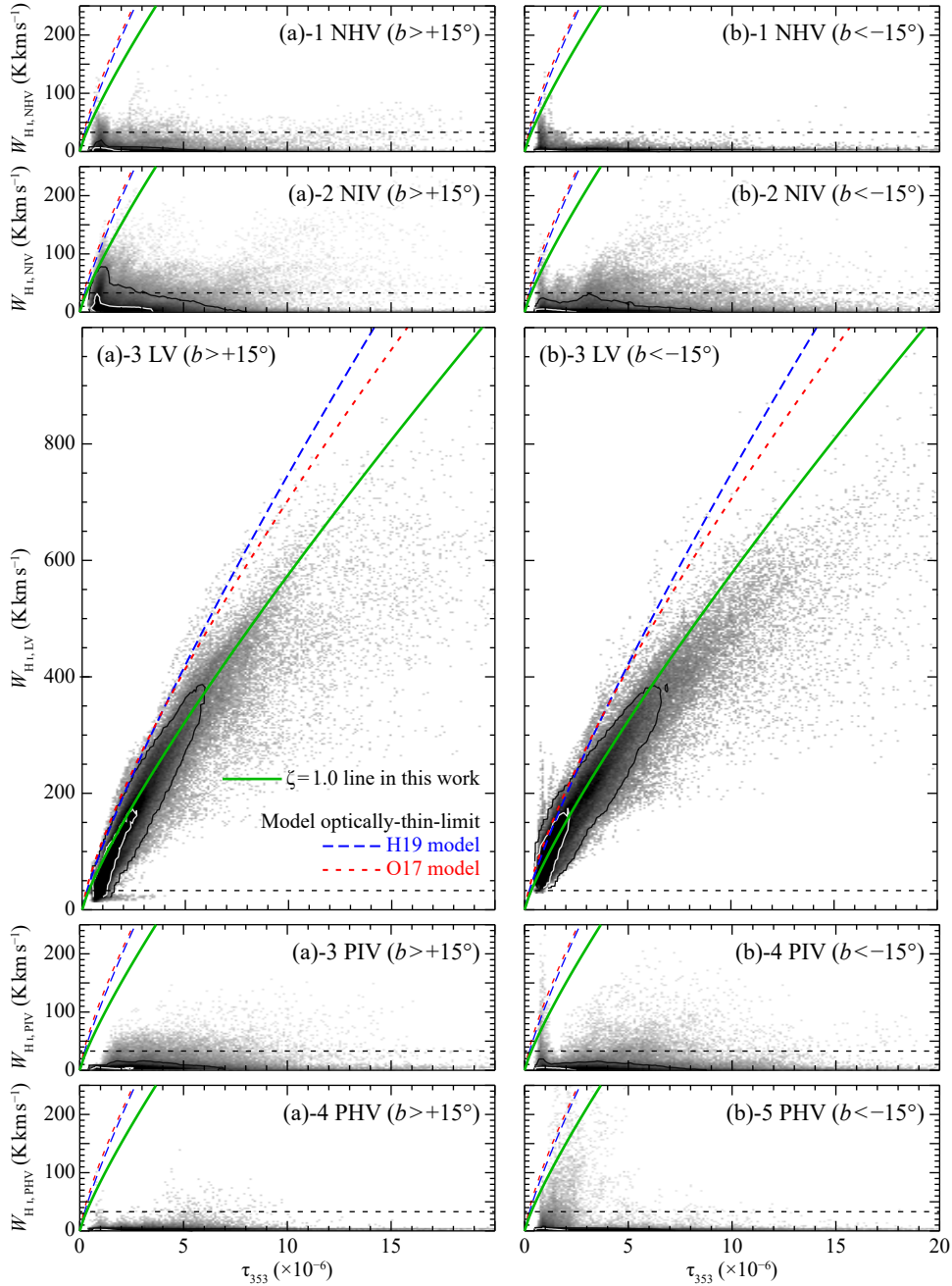


Figure 4. Density plots showing the correlation between τ_{353} and W_{HI} in the NHV, NIV, LV, PIV and PHV velocity ranges (from top to bottom). The W_{HI} values are obtained by integrating within each velocity range, but τ_{353} values are the total amount on the line-of-sights. The all masks described in Appendix A are applied. The panels in the left column are for $b > +15^\circ$ and those in the right column are for $b < -15^\circ$. The contours in each panel contain 50 and 90 per cent of data points. The green solid lines indicate the reference dust-to-gas ratio ($\zeta = 1.0$) line in this work $W_{\text{HI}} (\text{K km s}^{-1}) = (1.54 \times 10^{25}) / (1.82 \times 10^{18}) \times \tau_{353}^{1/1.2}$ (see text). The blue long dashed- and red short dashed lines indicate the optically-thin-limit line in the H19 model and the O17 model (see Section 4.1), respectively. The horizontal dashed line in each panel represents a threshold of $N_{\text{HI}}^* = 6 \times 10^{19} \text{ cm}^{-2}$ ($W_{\text{HI}} = 33 \text{ K km s}$), beyond which the ‘metallicity’ term ζ_X in equation (5) can be determined with $\sigma(\zeta_X) \lesssim 0.3$ (see Section 4.2 and Appendix D2).

$\zeta_X(l_i, b_i)$ as

$$\tau_{353}(l_i, b_i) = \left(\frac{C_0}{C}\right)^\alpha \sum_X [\zeta_X(l_i, b_i) W_{\text{HI},X}(l_i, b_i)]^\alpha, \quad (9)$$

where (l_i, b_i) are the galactic coordinates of the i -th data point ($i = 1, \dots, n$; $n = 4 \times 10^5$ in the present study).

4.2 Regression analysis and results

We estimated $\zeta_X(l_i, b_i)$ at each data point using the GWR technique. The traditional (ordinal) linear regression determines a set of global (spatially invariant) coefficients, whereas GWR estimates local regression coefficients at each data point employing a distance-decay weighting function. We used a truncated-Gaussian weighting

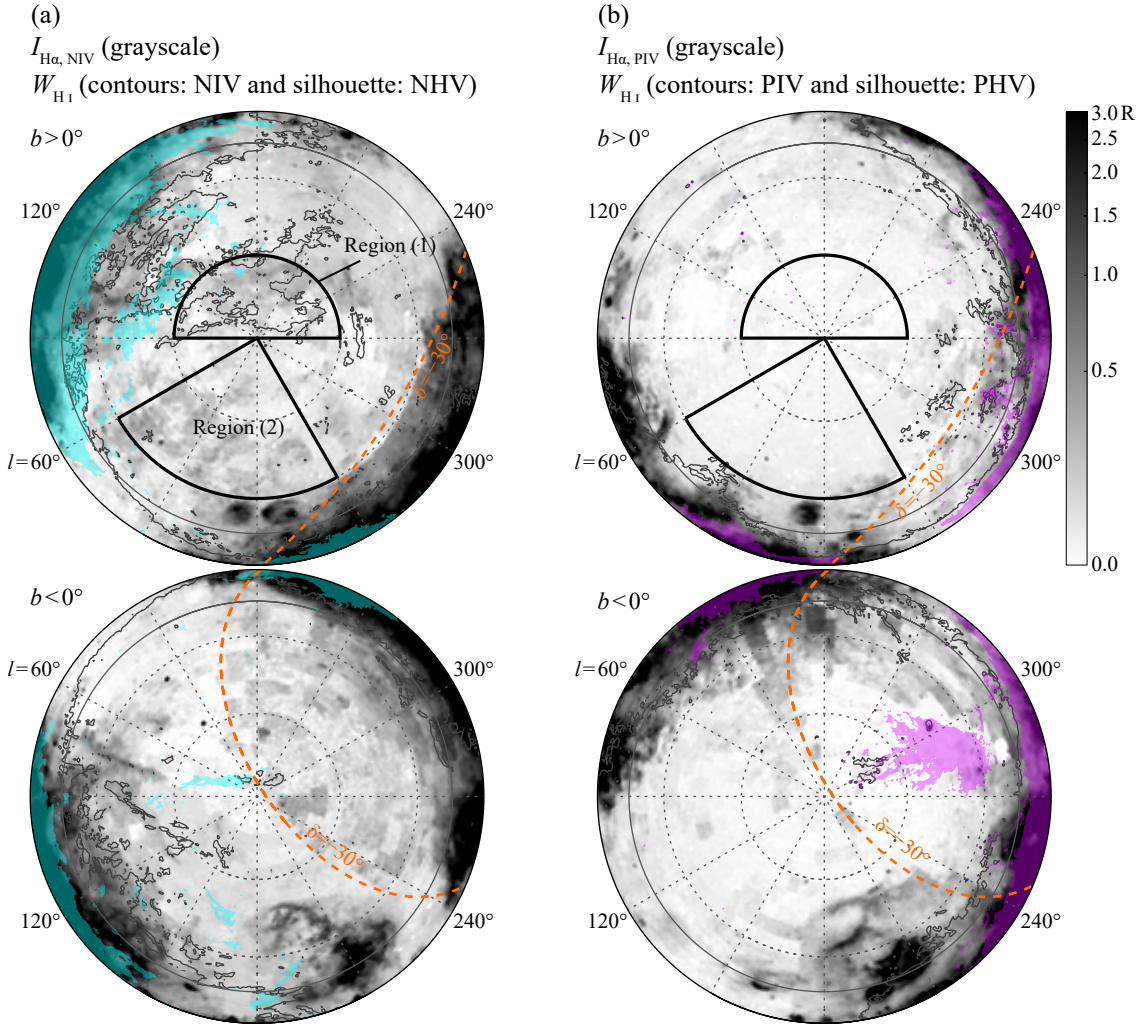


Figure 5. (a) The grayscale image shows the spatial distribution of H α intensity $I_{\text{H}\alpha}$ (Haffner et al. 2003, 2010) in the NIV velocity range shown in the same projection as Fig. 1. The southern limit of the WHAM-NSS (Haffner et al. 2003), $\delta = -30^\circ$, is presented by thick broken lines. The contours show $W_{\text{H}\text{I},\text{NIV}} = 30 \text{ K km s}^{-1}$ in the same velocity range, and the cyan silhouette shows the NHV H I components with $W_{\text{H}\text{I},\text{PHV}} > 10 \text{ K km s}^{-1}$. The gray solid lines indicate $|b| = 15^\circ$. The circular sectors bounded by thick solid lines present the two regions analyzed in Section 3.2. (b) Same as (a) but in the PIV velocity range. The contours show $W_{\text{H}\text{I},\text{PIV}} = 30 \text{ K km s}^{-1}$ and the magenta silhouette shows the PHV H I components with $W_{\text{H}\text{I},\text{PHV}} = 10 \text{ K km s}^{-1}$.

function

$$w_i(l_j, b_j) = \begin{cases} \exp\left[-\frac{1}{2}\left(\frac{\theta_{ij}}{\theta_{\text{bw}}}\right)^2\right] & (\theta_{ij} \leq \theta_{\text{tr}}) \\ 0 & (\text{otherwise}) \end{cases}, \quad (10)$$

where θ_{ij} is the great-circle angular distance between the regression point (the data point where we want to estimate the local coefficients $\zeta_X(l_i, b_i)$) and the j -th ($j = 1, \dots, n$) data point (l_j, b_j) , θ_{bw} is the bandwidth of the weighting function, and $\theta_{\text{tr}} = 3.71 \times \theta_{\text{bw}}$ is the truncation radius which gives a truncation value of $w_i(l_j, b_j) = 1 \times 10^{-3}$. We used $\theta_{\text{bw}} = 20 \text{ arcmin}$ (FWHM = 47 arcmin). The results of GWR are relatively insensitive to the choice of weighting function (e.g., Fotheringham et al. 2002); not only Gaussian but also, for example, bi-square functions are often used. Because the ζ_X values are not allowed to become negative, we introduced a non-negative least-squares (NNLS) regression technique in which ζ_X is set to 0 if the component X at and around a regression point has a very low dust-to-gas ratio. The procedures and formulae in the analysis are summarized in Appendices D.

Fig. 7 shows the spatial distribution of $\widehat{\zeta}_{\text{NHV}}$, $\widehat{\zeta}_{\text{NIV}}$, and $\widehat{\zeta}_{\text{LV}}$ (the hat symbol means that the variable is estimated by the regression), estimated by adopting ‘modified H19 model’ $C = 1.5 \times 10^{25} \text{ cm}^{-2}$ (chosen to the $W_{\text{H}\text{I},\text{LV}}$ -weighted mode of $\widehat{\zeta}_{\text{LV}}$ to be 1.0) and $\alpha = 1.2$. The remaining results of the analyses, $\widehat{\zeta}_{\text{PIV}}$ and $\widehat{\zeta}_{\text{PHV}}$, are presented in Appendix D. The standard error of $\widehat{\zeta}_X$, $\sigma(\widehat{\zeta}_X)$, is inversely proportional to $W_{\text{H}\text{I},X}$ (or $N_{\text{H}\text{I},X}^*$), but is not dependent on $\widehat{\zeta}_X$ (see Appendix D2). We hereafter set a threshold column density at $N_{\text{H}\text{I},X}^* = 6 \times 10^{19} \text{ cm}^{-2}$ ($W_{\text{H}\text{I},X} = 33 \text{ K km s}^{-1}$), beyond which $\widehat{\zeta}_X$ can be determined with $\sigma(\widehat{\zeta}_X) \lesssim 0.3$. We find that the total mass of the IVC gas is $1.5 \times 10^6 M_\odot$ (assuming a distance of 1 kpc, see below) and the metallicity is determined in the present work for 29 per cent of the IVC gas (Table 1).

Fig. 8 shows the metallicity distribution function (the distribution of the H I mass as a function of $\widehat{\zeta}_X$). The H I-mass at each pixel is given by

$$M_{\text{H}\text{I},X}(l, b) = C_0 m_p W_{\text{H}\text{I},X}(l, b) \frac{4\pi}{12N_{\text{side}}^2} D^2, \quad (11)$$

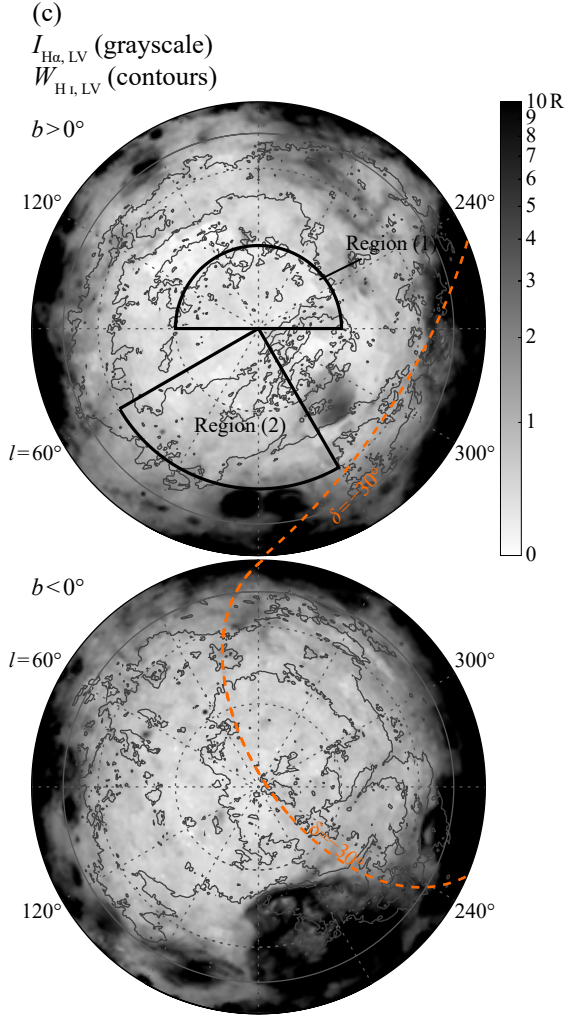


Figure 5 – continued (c) Spatial distribution of $I_{\text{H}\alpha}$ in the LV. The contours show $W_{\text{H I, LV}} = 30, 100,$ and 300 K km s^{-1} .

where (l, b) are the galactic coordinates of the pixel, m_p is the mass of the proton, $N_{\text{side}} = 256$ is the resolution parameter in the present dataset, and D is the distance to the H I gas. We applied $D = 150 \text{ pc}$ for the LV component, 1 kpc for the NIV component (excluding IV21 and the Magellanic Stream), and 10 kpc for the HVC Complex C.

We give a description of the properties of the LV, NIV and HVC and some of the individual objects in the following subsections.

4.2.1 The LV components

The LV components, considered to be the local gas in the solar vicinity, have a metallicity (\widehat{Z}_{LV}) range from 0.6 to 1.5 at 10 per cent of the peak level and the distribution is nearly Gaussian shape with a dispersion of 0.1 dex (Fig. 8(a)). The measurements of metallicity of G dwarfs were made for the local volume within 25 pc by many authors in the last five decades (e.g., Rocha-Pinto & Maciel 1996). These works indicate that the dispersion of metallicity is 0.2–0.3 dex with a peak at -0.2 dex. The dispersion is somewhat larger than the present one. Considering the much longer age of G dwarfs, several Gyr, than the dynamical timescale of H I gas, $\sim \text{Myr}$, the difference seems reasonable, and the H I gas in the local volume seems to be well mixed probably by the turbulent motion.

4.2.2 The NIV components

The metallicity of the IVCs in the NIV range, most of them are in the complexes the IV Arch and Spur, ranges from $\widehat{Z}_{\text{NIV}} = 0.2$ to 1.5 with a peak at 0.6, and 30 per cent of them have less than 0.5 (Fig. 8(b)). This result raises revision of the conventional view that the IVCs have metallicities nearly 1.0 solar, and may indicate an appreciable fraction of the IVCs originated in the low metallicity environment in the Galactic halo or further away. The IVCs are then not exclusively due to the Galactic-fountain picture but indicate a significant fraction of the falling gas from the Galactic halo or outside the Galaxy.

Fig. 9(a) shows that the metallicity of the IV Arch and Spur depends on velocity in the sense that the low-velocity IVCs tend to have higher metallicity. We find a trend that the high-velocity part lies in the inner part of the IV Arch and Spur and its low-velocity part in the outer part in Fig. 10. The typical infalling time scale of the IVCs is estimated to be $1 \text{ kpc}/100 \text{ km s}^{-1} \sim 10 \text{ Myr}$. The continuity of the IV Arch and Spur and the short time scale of the IVCs suggest that the metallicity of the IV Arch and Spur may be changing in $\sim 10 \text{ Myr}$. A possibility is that the IV Complex is dynamically interacting with the halo gas having high metallicity, and significant gas accretion onto the IV Arch and Spur is taking place. This accretion will make the IVCs decelerated and more massive. It is likely that the process also increases its metallicity by merging with high metallicity gas in the halo (T. Inoue, private communication). The process will be more important for smaller IVCs of $< 10^3 M_{\odot}$, while the interaction will not be effective for a massive IVC of $10^4 M_{\odot}$. The simulations by Shelton et al. (2022) dealt with such a massive IVC and deceleration does not seem to be significant.

4.2.3 IVC 86–36 and PP Arch

The recent result on IVC 86–36 in the head of PP Arch indicates a low metallicity of $\lesssim 0.2$ compared with the solar neighbor (F21). The present metallicity distribution for the PP Arch (Fig. 11) is not directly compared with F21 for the following reasons.

(i) The reference dust-to-gas ratio in F21 (the τ_{353} - $W_{\text{H I}}$ relationship for the foreground local ISM, their equation (3)) gives ~ 30 per cent smaller ‘metallicity’ values than those in the present study; the value of 0.22 in F21 corresponds to approximately $\widehat{Z}_{\text{NIV}} = 0.3$ in the present study. This should be because the foreground local H I in F21 is not optically thin enough, though they picked up the data points with high dust temperature ($T_d > 21 \text{ K}$).

(ii) In the present work, a large part of IVC 86–36 is masked due to saturated local H I emission (meet the criterion (d) in Appendix A), and a small number of data points are valid.

(iii) The uncertainties of the foreground-subtracted τ_{353} in F21 ($\sim 1 \times 10^{-6}$) are larger than the contribution of IVC 86–36 to τ_{353} (estimated to be 10^{-7}). F21 presented the low metallicity of IVC 86–36 but did not accurately obtain the regression coefficient of τ_{353} - $W_{\text{H I}}$ correlation in IVC 86–36.

In spite of that, the present result reveals that the tail of PP Arch has a low metallicity of $\widehat{Z}_{\text{NIV}} = 0.2$ and complements the low metallicity observed in the head. If the low metallicity is correct, the previous observations of the absorption lines toward the IVCs may be subject to errors due to uncertain ionization states of the atoms and/or the interstellar depletion.

Fig. 12, the velocity-metallicity plot in PP Arch, shows no dependence between the two parameters. This may be explained if the halo gas is less dense in the negative (Galactic southern) hemisphere, leading to less interaction than in the positive latitude.

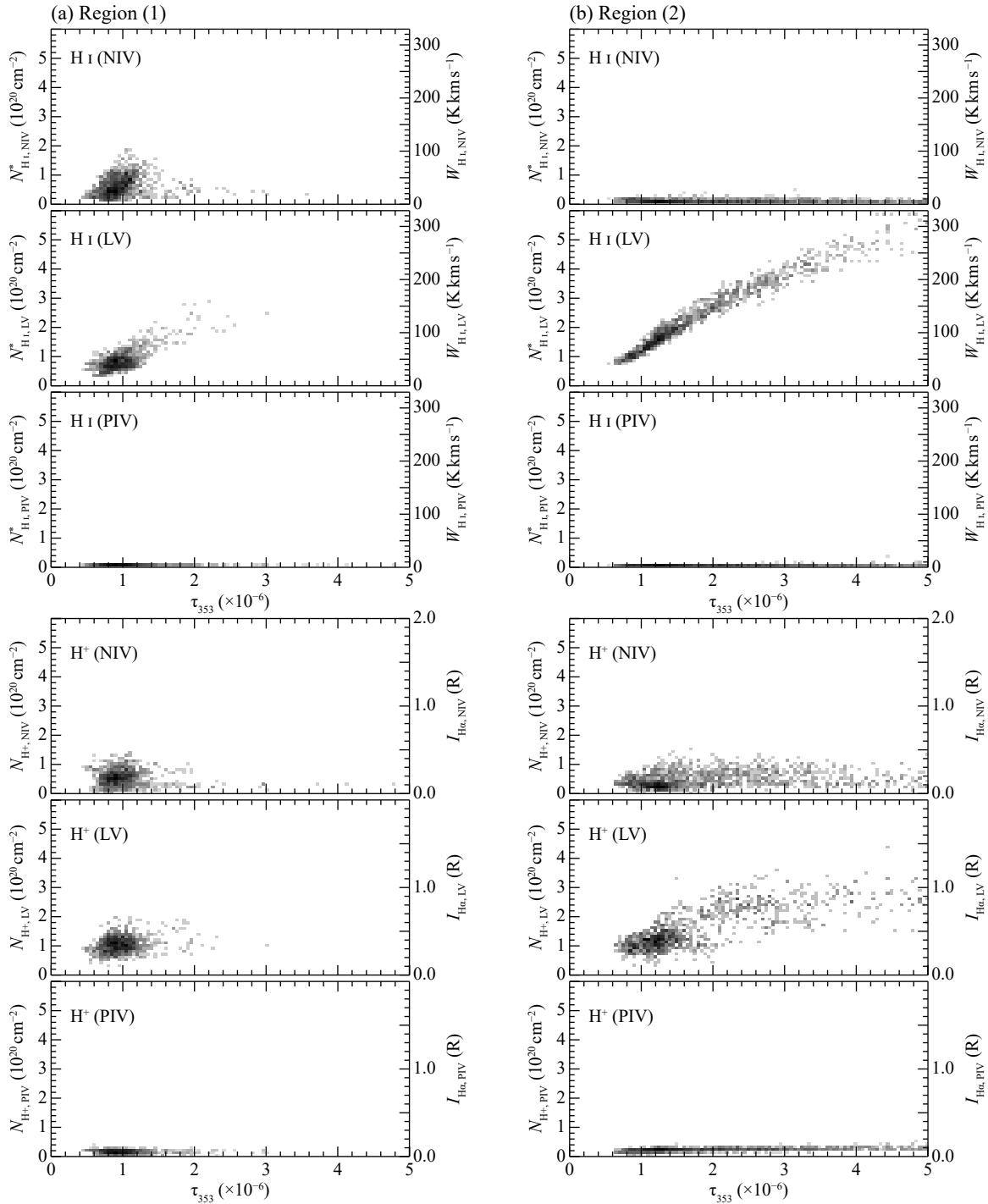


Figure 6. Density plots showing the τ_{353} - $N_{\text{H I}}^*$ and τ_{353} - N_{H^+} correlations in the NIV, LV, and PIV velocity ranges (from top to bottom), for (a) region (1) and (b) region (2) presented in Fig. 5. The $N_{\text{H I}}^*$ and N_{H^+} values are converted from $W_{\text{H I}}$ and $I_{\text{H}\alpha}$ ones (shown in the right-hand vertical axis in each panel). The $W_{\text{H I}}$ and $I_{\text{H}\alpha}$ are obtained within each velocity range, but τ_{353} values are the total amount on the line-of-sights.

4.2.4 The HVCs

Complex C has the largest apparent size among HVC complexes in $|b| > 15^\circ$ skies outside of the Magellanic Stream and barely enough column density to allow the present metallicity measurement. Fig. 8(c) indicates that the metallicity of the complex is significantly lower than that of the IVCs; 50 per cent of the HVCs show $\widehat{\zeta}_{\text{NHV}} < 0.2$ and 90 per cent show $\widehat{\zeta}_{\text{NHV}} < 0.5$. We find no strong dependence of

the metallicity on velocity (Fig. 9(b)). If we adopt the same interaction scheme, the no correlation may be explained as due to the lower gas density in the halo, because the HVCs are located at 10 kpc (Thom et al. 2008), further away from the plane.

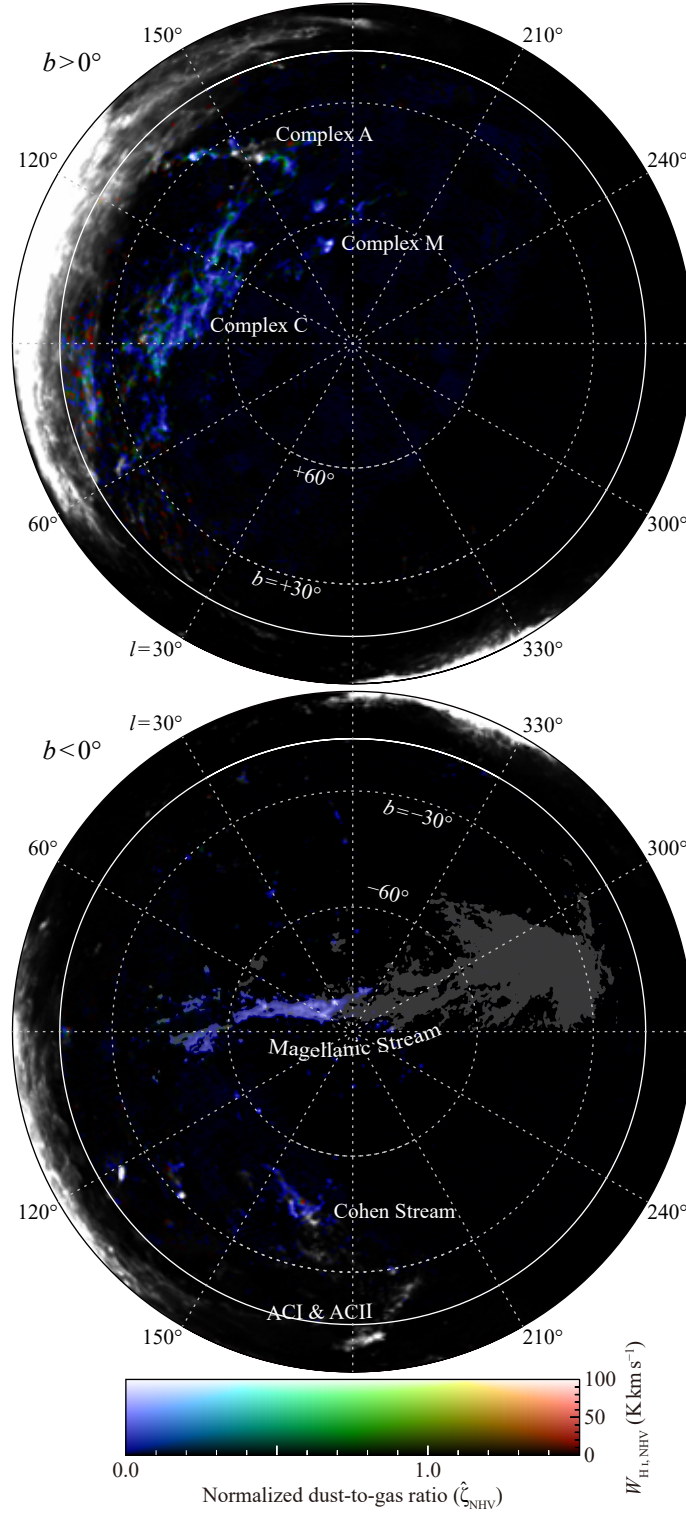


Figure 7. (a) Spatial distribution of $\widehat{\zeta}_{\text{NHV}}$ encoded as color hue (or grayed out if $\widehat{\zeta}_{\text{NHV}}$ are not available there) and $W_{\text{H I, NHV}}$ presented by brightness, shown in the same projection as Fig. 1. The gray shade in the lower panel outline the Magellanic Stream.

4.2.5 The Magellanic Stream

The Magellanic Stream is a $H\text{ I}$ streamer which was probably formed by the tidal interactions between the Magellanic Clouds and the Galaxy ~ 2 Gyr ago. According to the numerical simulations, most of the $H\text{ I}$ gas was stripped off from the Small Magellanic Cloud (SMC)

halo and it is expected that the gas has very low metallicity similar to the SMC (e.g., Besla et al. 2010). Figs. 13 and 8(d), the spatial distribution and the distribution function of $\widehat{\zeta}_X$ in the Magellanic Stream, indicate that the gas is of low metallicity even more than the HVCs, and 90 per cent of the gas has $\widehat{\zeta}_X < 0.15$. Tsuge et al. in prep. derived metallicity by the same method with F21 and derived

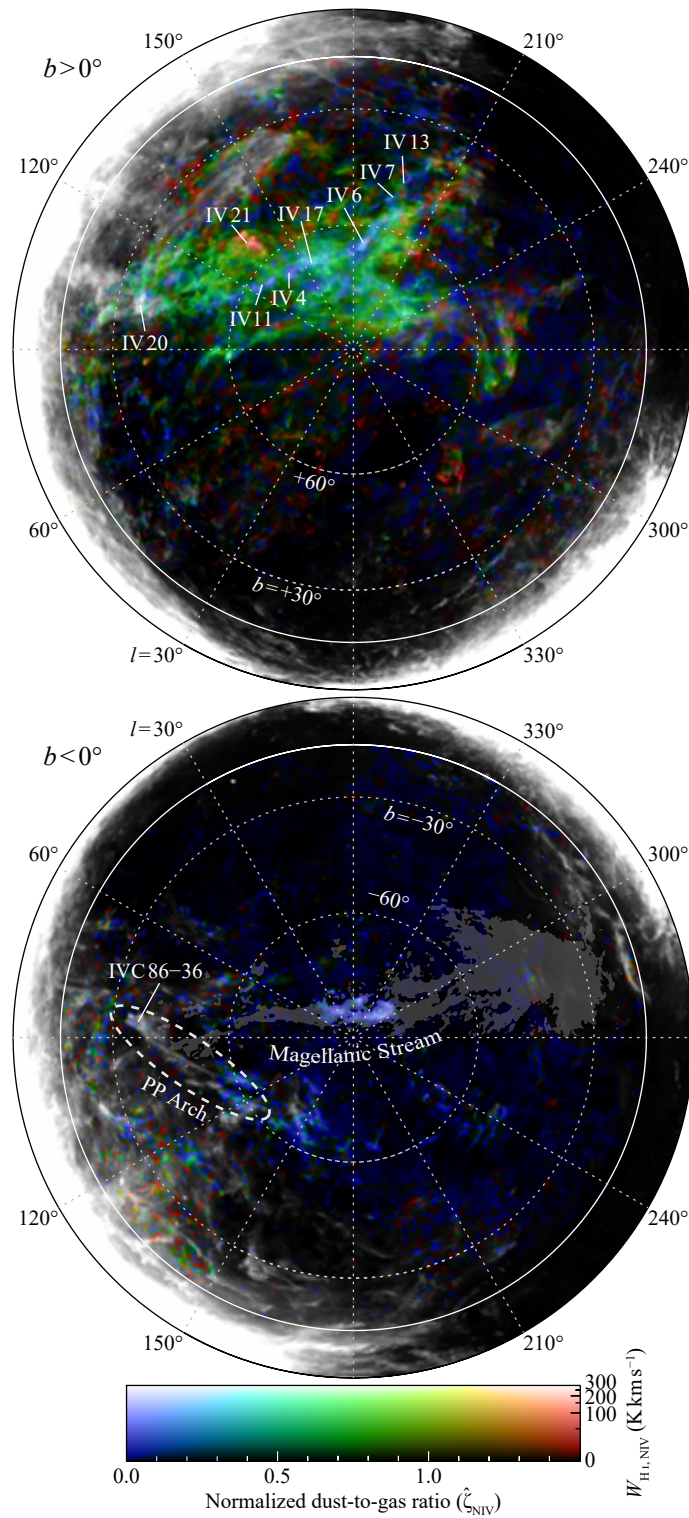


Figure 7 – continued (b) Same as (a) but for the NIV. Some of IVC clumps identified by [Kuntz & Danly \(1996\)](#) and some features are labeled.

the metallicity distributions. The results indicate that the SMC has a low metallicity similar to the Magellanic Stream, while the LMC contains more metal-rich gas than the Magellanic Stream.

5 DISCUSSION

5.1 Comparison of the present metallicity with the absorption line measurements

The present work revealed the metallicity distribution which covers a large fraction of the local ISM, the IVCs and the HVCs. We compare

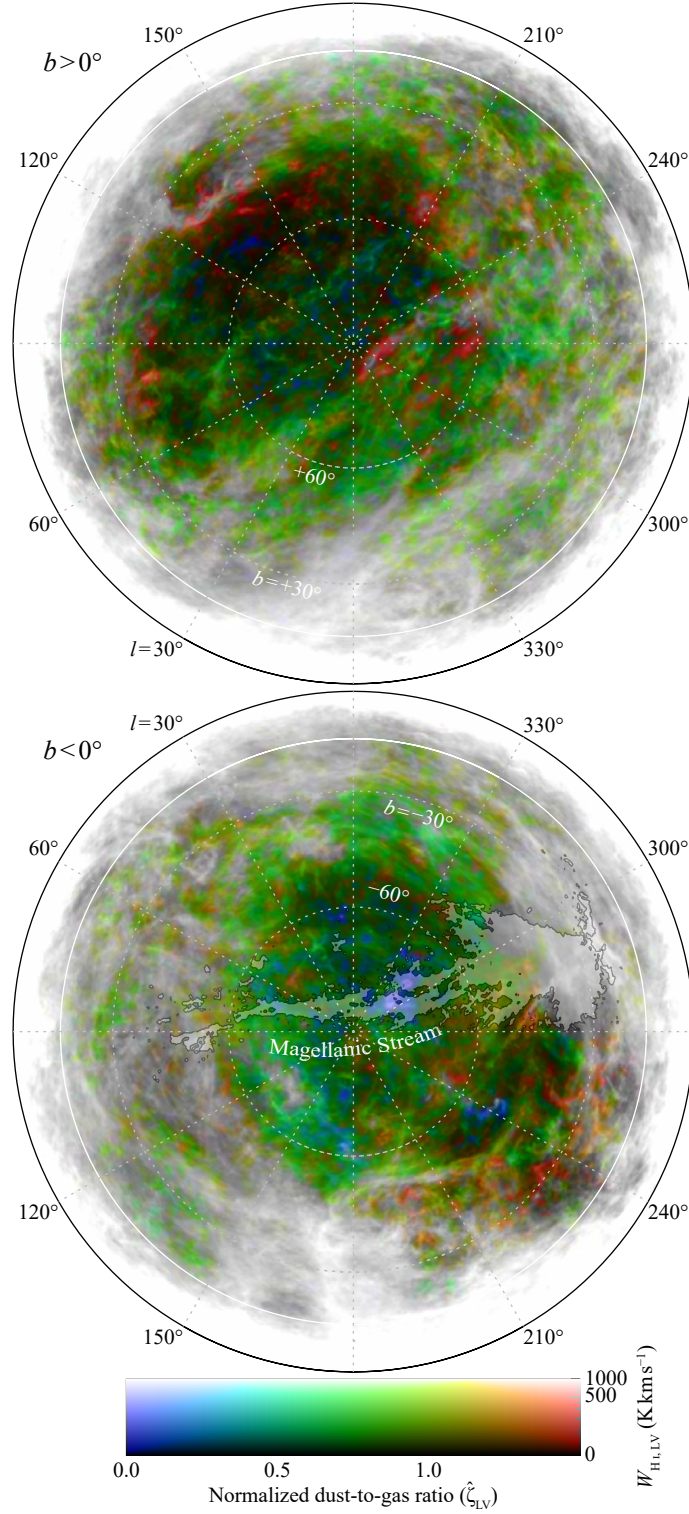


Figure 7 – *continued* (c) Same as (a) but for the LV.

the present results with the previous absorption line measurements in Table 2. Most of these absorption line measurements were made before 2001 and Wakker (2001) compiled the metallicity and the distance of the HVCs and IVCs comprehensively from the literature. Some limited number of measurements were made after that, while they do not affect the compilation. In table 4 of Wakker (2001);

the metallicity is ~ 0.1 solar for one HVC (Complex C), ~ 0.3 solar for the Magellanic Stream, ~ 0.5 solar for a southern IVC, and are consistent with \sim solar for two northern IVCs (the IV Arch and LLIV Arch) and three more IVCs. The effective resolution of the absorption measurements is given by a stellar image, and is extremely small as compared with the present resolution 47 arcmin.

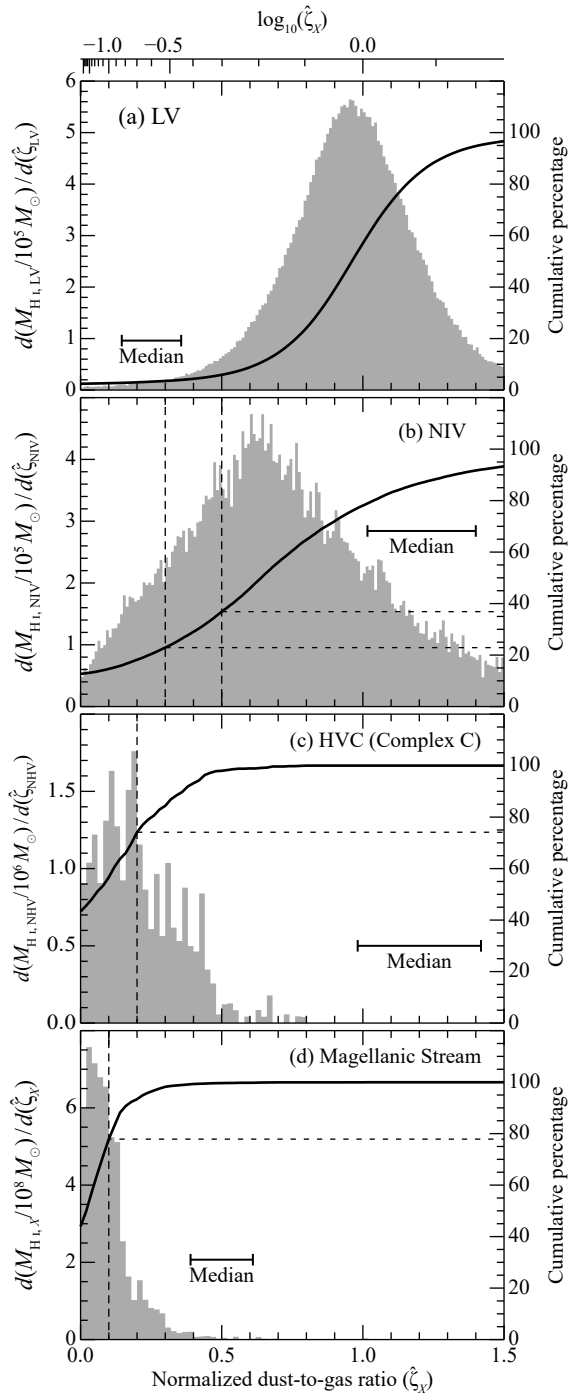


Figure 8. (a) Distribution of the H I mass as a function of $\widehat{\zeta}_{LV}$ for $N_{H I, LV}^* > 6 \times 10^{19} \text{ cm}^{-2}$ for the LV component (shown in the left-hand vertical-axis). The H I mass is estimated by equation (11) assuming a distance of $D = 150 \text{ pc}$. The solid line shows the cumulative percentage (right-hand vertical-axis). The horizontal bar shows the median of the uncertainties, $\sigma(\widehat{\zeta}_{LV})$. (b) Same as (a) but for the NIV component. The H I mass is estimated by assuming $D = 1 \text{ kpc}$. The vertical long dashed lines are $\widehat{\zeta}_{NIV} = 0.3, 0.5, \text{ and } 0.7$, and the horizontal short dashed lines are the cumulative percentages at the values. (c) Same as (a) for HVC Complex C ($l = 77^\circ - 140^\circ$, $b = +30^\circ - +60^\circ$, $V_{LSR} < -100 \text{ km s}^{-1}$). The H I mass is estimated by applying $D = 10 \text{ kpc}$ (Thom et al. 2008). The vertical dashed lines is $\widehat{\zeta}_{NIV} = 0.2$. (d) Same as (a) but for the Magellanic Stream. The H I mass is estimated by assuming $D = 55 \text{ kpc}$. The vertical dashed lines is $\widehat{\zeta}_X = 0.1$.

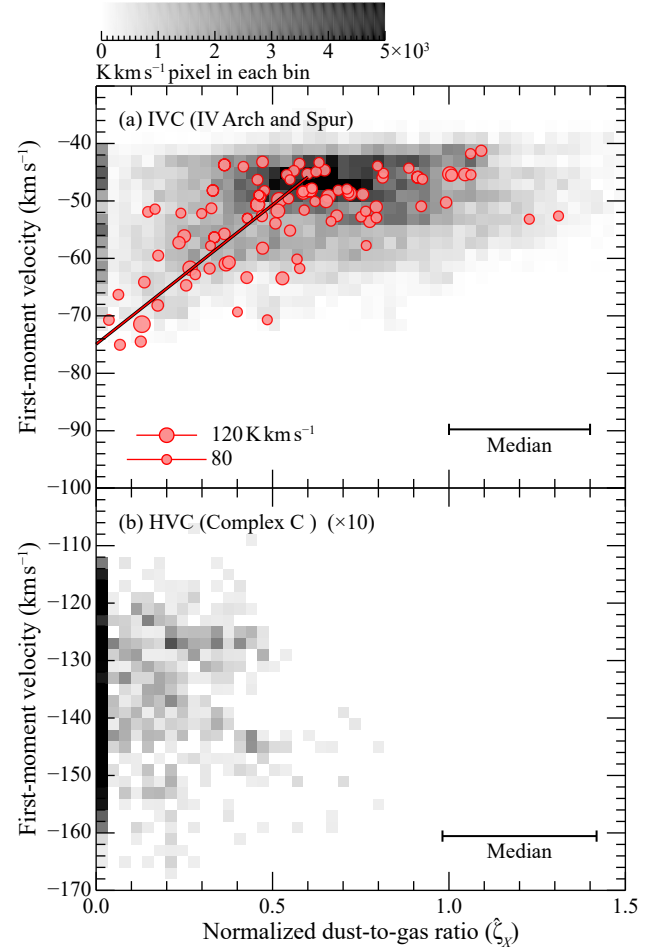


Figure 9. The image shows the $\widehat{\zeta}_X$ -first moment velocity (\bar{V}) distribution of (a) the IV Arch and Spur ($l = 90^\circ - 210^\circ$, $b > 45^\circ$) and (b) the HVC Complex C ($l = 77^\circ - 140^\circ$, $b = +30^\circ - +60^\circ$), weighted with $W_{H I, X}$ ((b) is multiplied by 10). The data points with $N_{H I, X}^* > 6 \times 10^{19} \text{ cm}^{-2}$ are used, and the horizontal bar in the bottom-right corner of each panel shows the median of the uncertainties $\sigma(\widehat{\zeta}_X)$ for the data points. The overlaid bubble plot in panel (a) presents the $\widehat{\zeta}_{NIV} - \bar{V} - W_{H I, NIV}$ for data points with $W_{H I, NIV} > 80 \text{ K km s}^{-1}$ (only 100 randomly selected points are shown), and the solid line is a linear regression by an ordinary least squares (OLS)-bisector method (Isobe et al. 1990), $\bar{V} (\text{km s}^{-1}) = (48.5 \pm 0.2)\widehat{\zeta}_X - (74.9 \pm 0.1)$ ($\widehat{\zeta}_{NIV} < 0.6$).

So, the two metallicity values sample entirely different volume, which differs by many orders of magnitude, and the values of the absorption measurements must be subject to large fluctuations due to the small volume. In spite of that we find that the low metallicity of $\sim 0.1 - 0.3$ solar in the HVCs and the Magellanic Stream is fairly consistent with the present results. Further, the metallicity is given to be 0.54 ± 0.04 solar in the IVC PP Arch and to be ~ 1 solar in the rest of the IVCs. These IVC values, $0.5 - 1.0$ solar, are consistent with the distribution of the metallicity in Figure 8(b), which shows that for 60 per cent of the IVCs the metallicity is distributed in a range from $\widehat{\zeta}_{NIV} = 0.5$ to 1.5 with a $M_{H I, NIV}$ -weighted mode at 0.6. We therefore conclude that the absorption measurements show reasonable consistency with the present metallicity distribution function.

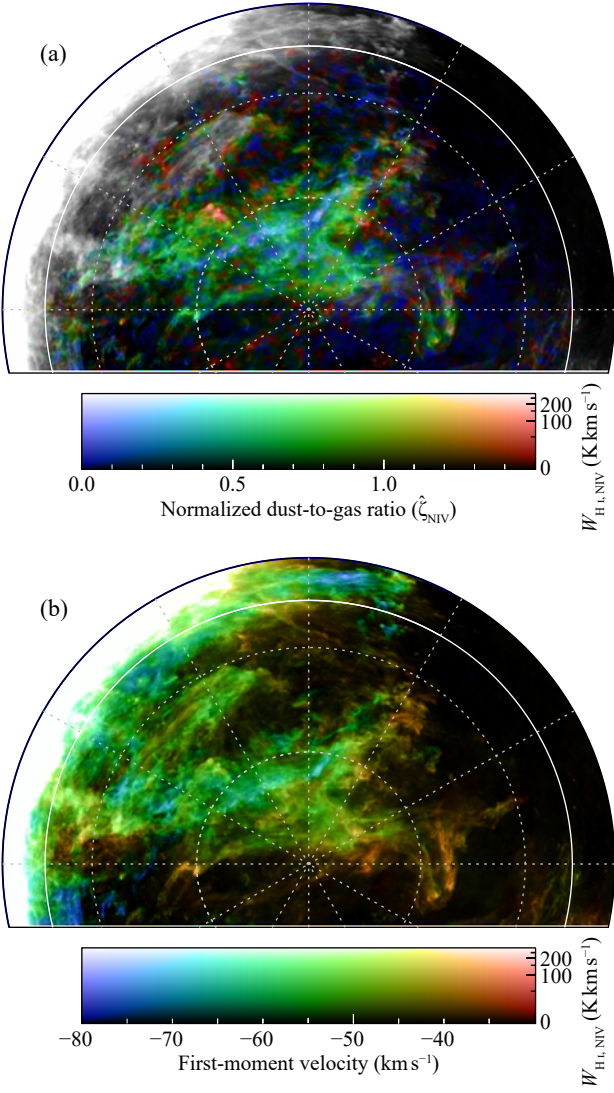


Figure 10. (a) A close-up view of Fig. 7(b), centered on IV Arch and Spur. (b) Spatial distribution of the first-moment velocity in $V_{\text{LSR}} = -100$ – -30 km s^{-1} encoded as color hue and $W_{\text{HI,NIV}}$ presented by brightness in the same area as panel (a).

5.2 The effect of the dust transformation

The dust may be subject to physical/chemical transformation and have the different emission properties in the neutral gas in the Local Group. The shock waves with velocity higher than 100 km s^{-1} are shown to be the most efficient dust destruction process according to previous theoretical works (e.g., Jones 2004). Such high velocity shock waves are usual in supernova remnants. Also, the IVCs and HVCs having high velocity around 100 km s^{-1} may ionize the gas as observed by the H α emission toward the IVCs. Comparison of the H α emission with τ_{353} indicates that such ionized gas contains little dust as argued in Section 3.2. This is likely due to the dust destruction by grain-grain sputtering in the high velocity collision. The neutral gas inside the HVCs may not be affected much by the shocks because the shock velocity is probably retarded inside the IVCs. This in fact seems to be consistent with the relatively loose correlation between H α and the intense parts of NIV; e.g., IVC 86–36 shows no clear enhancement of H α as compare with the whole PP Arch (see Figure 5(a)), while some

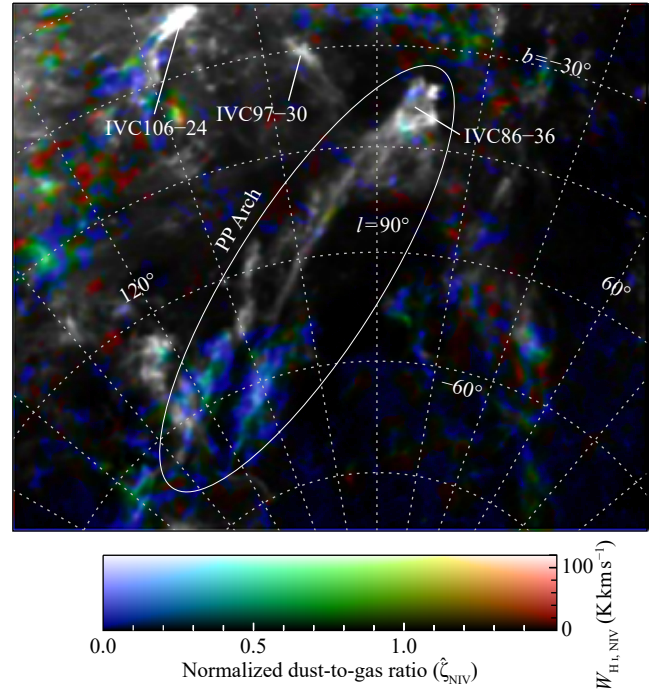


Figure 11. A close-up view of Fig. 7(b), centered on PP Arch including IVC 86–36.

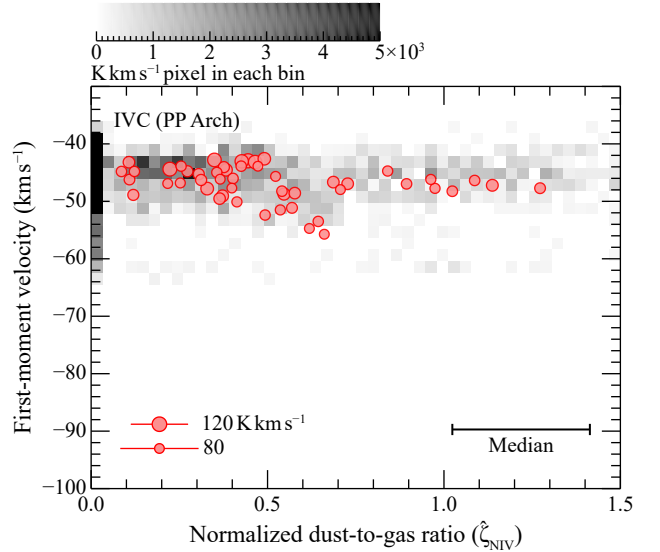


Figure 12. The image shows the $\hat{\zeta}_{\text{NIV}} - \bar{V}$ distribution of the PP Arch ($l = 80^\circ$ – 150° , $b = -75^\circ$ – -30°), weighted with $W_{\text{HI,NIV}}$ (multiplied by 5). The data points with $N_{\text{HI,NIV}}^* > 6 \times 10^{19} \text{ cm}^{-2}$ are used, and the horizontal bar in the bottom-right corner of each panel shows the median of the uncertainties $\sigma(\hat{\zeta}_{\text{NIV}})$ for the data points. The overlaid bubble plot presents the $\hat{\zeta}_{\text{NIV}} - \bar{V} - W_{\text{HI,NIV}}$ plot for data points with $W_{\text{HI,NIV}} > 80 \text{ K km s}^{-1}$.

IVCs having less H I column density might be more highly ionized. So, we infer that the dust transformation is probably not so important in the present measurements, which focus on $N_{\text{HI}}^* > 6 \times 10^{19} \text{ cm}^{-2}$ (the vertical lines in Figure 2), while future extensive follow-up works including the shock interaction of IVCs and HVCs will be valuable to ensure better the present metallicity measurements.

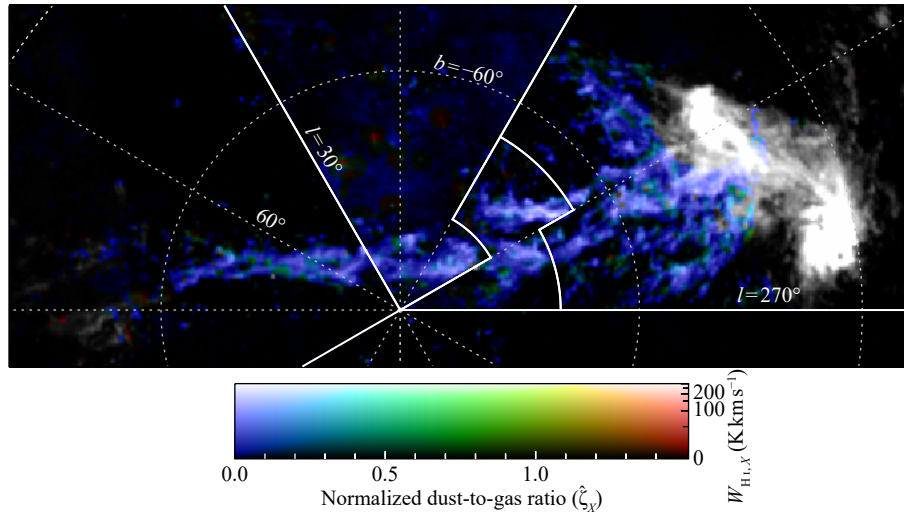


Figure 13. A patchwork of the NHV, NIV, PIV, and PHV maps showing the spatial distribution of $\widehat{\zeta}_X$ (color) and $W_{\text{H I},X}$ (brightness) in the Magellanic Stream.

Table 2. Summary of metallicities.

Cloud	Metallicity ^a (Relative to Solar)	$\widehat{\zeta}_X$ ^b
HVCs (in NHV)		
Complex A	0.02 – 0.04	0 – 0.3
Complex C	$0.089 \pm 0.024^{+0.020}_{-0.005}$	0 – 0.2
IVCs (in NIV)		
IV Arch and Spur	~ 1	0.4 – 0.9
LLIV Arch	1.0 ± 0.5	...
PP Arch	0.54 ± 0.04	0 – 0.7
Magellanic Stream (tail)	0.33 ± 0.05	0 – 0.08

^a Taken from table 4 of [Wakker \(2001\)](#).

^b The $N_{\text{H I},X}^*$ -weighted 25h and 75th percentiles of $\widehat{\zeta}_X$ for data points with $N_{\text{H I},X}^* > 6 \times 10^{19} \text{ cm}^{-2}$.

5.3 The HVCs and IVCs, their interaction with the halo

The origin and connection of the IVCs and HVCs have been an issue of broad interest over several decades since [Oort \(1966\)](#). According to the literature (e.g., [Wakker 2001](#)), it is favored that the IVCs are mostly originated by the Galactic-fountain mechanism within the Galaxy, and that the HVCs are of the extragalactic origin. As discussed in Section 5.1 the Galactic origin of the IVCs is suggested by the higher metallicity of the IVCs, 0.5 – 1.0 solar, than the HVCs, which was derived by the absorption measurements. The present results, with orders of magnitude larger spatial coverage, revealed that the IVCs have significantly lower metallicity than previously thought (more than 35 per cent of the IVCs are $\widehat{\zeta}_{\text{NIV}} < 0.5$). Another intriguing aspect revealed by the present work is that the metallicity of the IVCs shows a correlation with the velocity (Fig. 9(a)); the higher velocity IVCs at $< -50 \text{ km s}^{-1}$ have lower metallicity $\widehat{\zeta}_{\text{NIV}} < 0.5$, while the lower velocity IVCs at $> -50 \text{ km s}^{-1}$ have higher metallicity of $\widehat{\zeta}_{\text{NIV}} = 0.5 - 1.0$. These raise a possibility that at least part of the IVCs may be of extragalactic origin in a similar way to the HVCs. We also pay attention to that some IVCs show a strong sign of interaction with the halo gas. IVC 86–36 in PP Arch is located

at $z \sim 1 \text{ kpc}$ and shows kinematical bridge features between the IVC and the disk H I ([F21](#)). The bridge features seem to link the two H I gases as a result of the momentum exchange between them. A collision between two clouds is numerically simulated (e.g., [Takahira et al. 2014](#)) and the formation of such a bridge is demonstrated.

Motivated by these newly found properties, we frame a scenario that the IVCs are infalling to the disk from $z >$ several kpc under significant dynamical interaction with the halo gas. Possible consequences of the scenario are as follows. First, this scenario explains the dominant low metallicity of the IVCs. Second, the metallicity trend depending on velocity is explained in terms of accumulation of the high metallicity halo gas onto the IVC. [Henley et al. \(2017\)](#) and [Gritton et al. \(2014\)](#) presented a picture by hydrodynamical numerical simulations that HVCs/IVCs interact with the high metallicity halo gas, which mixes with the low metallicity HVC gas. The Smith cloud which is falling to the plane has high metallicity of 0.5 solar ([Fox et al. 2016](#)), and may be explained by such mixing. This issue affects deeply the interpretation of the metallicity of the IVCs and HVCs, and deserves further intensive pursuits.

As for the connection of the IVCs with the HVCs, it is possible that the HVCs evolve to the IVCs by the interaction with the low density gas outside the disk over 10 kpc, although the details of the halo gas is poorly constrained at present. In this scenario, an implication is that the total mass and the metallicity of the IVCs may be increased significantly by the accumulation of the halo gas. If so, the observed IVCs give an upper limit in mass for the real infalling gas outside the halo. This issue needs to be more carefully pursued by employing numerical simulations of the interaction and a detailed study of the IVC distribution and kinematics, which are beyond the scope of the present work.

Recent numerical simulations by [Shelton et al. \(2022\)](#) were aimed at numerically reproducing the formation of the long tail of PP Arch with a head IVC 86–36 observed by [F21](#). These authors reproduced the shape and revealed details of the physical processes of the interaction between an infalling cloud and the halo and disk. It showed that over 1 kpc the head develops a kpc long tail in the direction of its orbit making an angle nearly 45° to the plane. The cloud mass and the initial velocity is taken to be $10^4 M_\odot$ and 100 km s^{-1} respectively. In the end, the cloud completely merges with the disk, suggesting that most of the IVCs with less mass will merge with the disk. The

simulations of the Smith cloud show that the cloud having $10^6 M_{\odot}$ punches through the disk, and may be moving up and down through the disk (Fox et al. 2016; Lockman et al. 2008). We suggest that most of the IVCs having small mass less than $10^4 M_{\odot}$ will merge with the disk, as the Smith cloud as an exceptional case.

5.4 The G-dwarf problem and sustainment of the star formation rate

The IVCs are relevant to the long-standing issue, the G-dwarf problem (e.g., van den Bergh 1962; Pagel & Patchett 1975). The G-dwarf problem raised a dilemma that the metallicities of the G dwarfs in the Galaxy show no particularly low metallicity in spite of their old age in the order of 10 Gyr. In such an early area, G dwarfs should have significantly lower metallicity than the solar metallicity, if the metallicity of the ISM increases monotonically in time. The problem has also been observed in K and M dwarfs (e.g., Flynn & Morell 1997; Woolf & West 2012). A possible scenario to solve the problem is that the low metallicity gas is being supplied to the Galaxy continuously after the formation of the high-metallicity G dwarfs. Another issue relevant is that the current star formation rate of the Galaxy, $1 M_{\odot} \text{ yr}^{-1}$, may not hold as it is if the Galaxy received no additional gas supply from outside. This is because the total gas in the Galaxy will be consumed by star formation within several Gyr ago unless the Galaxy has no additional gas supply. If so, the current high star formation cannot be explained due to the lack of $H\text{ I}$ gas.

As has been discussed previously, the present findings have the potential to support the low-metallicity mass supply in the required order of magnitude as IVCs falling to the Galaxy. The $H\text{ I}$ mass of the present IVCs is estimated to be $1.5 \times 10^6 M_{\odot}$ within ~ 1 kpc of the sun (Table 1). Most of the IVCs have negative velocities. If we assume that all the IVCs are falling to the Galactic Disk at $\sim 100 \text{ km s}^{-1}$, the mass accretion rate within the 1 kpc radius of the sun is calculated to be $\sim 10^{-1} M_{\odot} \text{ yr}^{-1}$ for a typical dynamical time scale of the IVCs, ~ 10 Myr. This is a significant fraction of the total star formation rate of the Galaxy, $\sim 1 M_{\odot} \text{ yr}^{-1}$. As discussed above, the observed mass of the IVCs is probably an upper limit by considering the possible mass accumulation from the halo. If we assume that the net mass inflow occurs roughly in a 10 kpc radius, the mass accretion rate becomes $\sim 10 M_{\odot} \text{ yr}^{-1}$. This is able to supply the required low metallicity mass as discussed above even if the subsequent mass increase of the IVCs in the halo is considered. This issue will be pursued more deeply by an extensive analysis of the distribution and kinematics of the IVCs in the Galaxy and the nearby galaxies like M31 in future. The forthcoming new instruments including SKA and ngVLA are expected to provide important opportunities in these studies by covering the Local Group galaxies as well as nearby and more distant galaxies.

6 CONCLUSIONS

Aiming at revealing the metallicity distribution of the local ISM, the IVCs, and HVCs, we have carried out a multiple regression analysis of the 21 cm $H\text{ I}$ emission combined with the sub-mm dust emission τ_{353} over 29 per cent of the IVCs, for which we have derived the metallicity distribution most extensively. As byproducts, we obtained the metallicity distributions in the low-velocity gas in the solar vicinity, some of the HVCs, and the Magellanic Stream. The main conclusions are summarized below.

- (i) The analysis yields the dust-to-gas ratio of the multiple $H\text{ I}$

components including the IVCs, the HVCs, the Magellanic Stream, and the local interstellar medium outside the Galactic plane at an effective resolution of 47 arcmin, which is optimized for the multiple component analysis. The method covers the sky contiguously, and is distinguished from the conventional optical absorption line measurements toward bright stars which cover a very small fraction of the gas with uncertainties due to the atomic ionization states and the interstellar depletion. On the assumption that the dust-to-gas ratio is proportional to the metallicity, we derived the metallicity distribution function of all the components.

- (ii) The present study allowed us to derive the metallicity over a far greater portion of the $H\text{ I}$ gas than the previous studies, besides the IVCs, these include ~ 10 per cent of the HVC, most of the Magellanic Stream, and 43 per cent of the local ISM. The major results include that the metallicity of the IVCs varies from < 0.2 to 1.0 of the reference local ISM, and that a significant fraction, ~ 36 per cent of the IVCs includes the low metallicity gas of < 0.5 with a $H\text{ I}$ -mass weighted mode at 0.6. In addition, it is shown that the HVCs in Complex C has metallicity of < 0.1 of the reference local ISM, and that the Magellanic Stream has a uniform metallicity of < 0.2 . We argue that a large fraction of the low metallicity IVC gas is consistent with a picture of the external $H\text{ I}$ gas accretion of low metallicity as opposed to the Galactic-fountain model. It is likely that most of the IVCs merge with the Galactic $H\text{ I}$ disk and supply thereby the low metallicity gas at a rate of $\sim 10 M_{\odot} \text{ yr}^{-1}$, which may offer a solution of the G-dwarf problem and the gas deficiency to sustain star formation in the Galaxy.

- (iii) We find a trend observed in the IVCs, IV Arch and Spur, that the metallicity of the IVCs increases with decrease of velocity. We present a scenario where the IVCs are falling onto the Galactic plane and interacting with the high metallicity gas in the halo. The interaction is evidenced by the kinematic bridge features connecting the IVC with the disk in IVC 86–36 in PP Arch, and will cause accretion of the halo gas onto the IVCs. The accretion increases the metallicity and mass of the IVCs and decelerates their infall velocity. This scenario explains the observed correlation between the metallicity and velocity. The observed metallicity of the IVCs therefore gives upper limits for the metallicity and mass of the original infalling gas, suggesting that the original metallicity of the IVCs is even lower than derived.

In order to pursue further the implications of the IVCs, we need more systematic studies of the $H\text{ I}$ gas over the whole sky by focusing on the individual regions as well as the overall properties of the IVCs and HVCs. The forthcoming new instruments including SKA and ngVLA are expected to provide important opportunities in these studies by covering the Local Group galaxies as well as nearby and more distant galaxies.

ACKNOWLEDGEMENTS

This work was supported by JSPS KAKENHI Grant Numbers 15H05694 and 21H00040. This research made use of ds9, a tool for data visualization supported by the Chandra X-ray Science Center (CXC) and the High Energy Astrophysics Science Archive Center (HEASARC) with support from the JWST Mission office at the Space Telescope Science Institute for 3D visualization. EBHIS is based on observations with the 100-m telescope of the MPIfR (Max-Planck-Institut für Radioastronomie) at Effelsberg. The Parkes Radio Telescope is part of the Australia Telescope which is funded by the Commonwealth of Australia for operation as a National Facility managed by CSIRO. Some of the results in this paper have been derived

using the HEALPIX (Górski et al. 2005) package. The useful comments by T. Onishi, K. Tachihara and T. Inoue helped to improve the comment and readability of the paper.

DATA AVAILABILITY

The HI4PI data underlying this article are available in Vizier at <http://cdsarc.u-strasbg.fr/viz-bin/qcat?J/A+A/594/A116>. The *Planck* data are in Planck Legacy Archive (PLA) at <https://pla.esac.esa.int/>. The WHAM-SS data were available at <http://www.astro.wisc.edu/wham-site/wham-sky-survey/wham-ss/> until 2022 March, but the web site is inaccessible as is 2022 August. The data products from this study will be shared on reasonable request to the corresponding author.

REFERENCES

- Adams W. S., 1949, *ApJ*, **109**, 354
- Barger K. A., Haffner L. M., Wakker B. P., Hill A. S., Madsen G. J., Duncan A. K., 2012, *ApJ*, **761**, 145
- Berkhuijsen E. M., Müller P., 2008, *A&A*, **490**, 179
- Besla G., Kallivayalil N., Hernquist L., van der Marel R. P., Cox T. J., Kereš D., 2010, *ApJ*, **721**, L97
- Blaauw A., Tolbert C. R., 1966, *Bull. Astron. Inst. Netherlands*, **18**, 405
- Bregman J. N., 1980, *ApJ*, **236**, 577
- Brunsdon C., Fotheringham A. S., Charlton M. E., 1996, *Geographical Analysis*, **28**, 281
- Collins J. A., Shull J. M., Giroux M. L., 2003, *ApJ*, **585**, 336
- Dobler G., Draine B., Finkbeiner D. P., 2009, *ApJ*, **699**, 1374
- Finkbeiner D. P., 2003, *ApJS*, **146**, 407
- Fitzpatrick E. L., Spitzer Lyman J., 1997, *ApJ*, **475**, 623
- Flynn C., Morell O., 1997, *MNRAS*, **286**, 617
- Fotheringham A. S., Brunsdon C., Charlton M., 2002, *Geographically Weighted Regression: the analysis of spatially varying relationships*. Wiley
- Fox A. J., et al., 2016, *ApJ*, **816**, L11
- Fukui Y., et al., 2014, *ApJ*, **796**, 59
- Fukui Y., Torii K., Onishi T., Yamamoto H., Okamoto R., Hayakawa T., Tachihara K., Sano H., 2015, *ApJ*, **798**, 6
- Fukui Y., Tsuge K., Sano H., Bekki K., Yozin C., Tachihara K., Inoue T., 2017, *PASJ*, **69**, L5
- Fukui Y., et al., 2021, *PASJ*, **73**, S117
- Gaensler B. M., Madsen G. J., Chatterjee S., Mao S. A., 2008, *Publ. Astron. Soc. Australia*, **25**, 184
- Gómez G. C., Benjamin R. A., Cox D. P., 2001, *AJ*, **122**, 908
- Górski K. M., Hivon E., Banday A. J., Wandelt B. D., Hansen F. K., Reinecke M., Bartelmann M., 2005, *ApJ*, **622**, 759
- Gritton J. A., Shelton R. L., Kwak K., 2014, *ApJ*, **795**, 99
- HI4PI Collaboration 2016, *A&A*, **594**, A116
- Haffner L. M., Reynolds R. J., Tufte S. L., 2001, *ApJ*, **556**, L33
- Haffner L. M., Reynolds R. J., Tufte S. L., Madsen G. J., Jaehnig K. P., Percival J. W., 2003, *ApJS*, **149**, 405
- Haffner L. M., et al., 2010, in Kothes R., Landecker T. L., Willis A. G., eds, *Astronomical Society of the Pacific Conference Series Vol. 438, The Dynamic Interstellar Medium: A Celebration of the Canadian Galactic Plane Survey*. p. 388 ([arXiv:1008.0612](https://arxiv.org/abs/1008.0612))
- Hayashi K., Okamoto R., Yamamoto H., Hayakawa T., Tachihara K., Fukui Y., 2019a, *ApJ*, **878**, 131
- Hayashi K., et al., 2019b, *ApJ*, **884**, 130
- Henley D. B., Gritton J. A., Shelton R. L., 2017, *ApJ*, **837**, 82
- Hernandez A. K., Wakker B. P., Benjamin R. A., French D., Kerp J., Lockman F. J., O’Toole S., Winkel B., 2013, *ApJ*, **777**, 19
- Howk J. C., Savage B. D., 1999, *ApJ*, **517**, 746
- Isobe T., Feigelson E. D., Akritas M. G., Babu G. J., 1990, *ApJ*, **364**, 104
- Jones A. P., 2004, in Witt A. N., Clayton G. C., Draine B. T., eds, *Astronomical Society of the Pacific Conference Series Vol. 309, Astrophysics of Dust*. p. 347
- Jones A. P., Tielens A. G. G. M., Hollenbach D. J., McKee C. F., 1994, *ApJ*, **433**, 797
- Kalberla P. M. W., Haud U., 2015, *A&A*, **578**, A78
- Kalberla P. M. W., Burton W. B., Hartmann D., Arnal E. M., Bajaja E., Morras R., Pöppel W. G. L., 2005, *A&A*, **440**, 775
- Karachentsev I. D., Makarov D. I., Kaisina E. I., 2013, *AJ*, **145**, 101
- Kuntz K. D., Danly L., 1996, *ApJ*, **457**, 703
- Lagache G., Haffner L. M., Reynolds R. J., Tufte S. L., 2000, *A&A*, **354**, 247
- Lawson C. L., Hanson R. J., 1995, *Solving least squares problems*. SIAM, Philadelphia, PA, doi:<https://doi.org/10.1137/1.9781611971217>
- Lehner N., Howk J. C., 2011, *Science*, **334**, 955
- Lehner N., Howk J. C., Marasco A., Fraternali F., 2022, *MNRAS*,
- Lenz D., Kerp J., Flöer L., Winkel B., Boulanger F., Lagache G., 2015, *A&A*, **573**, A83
- Lockman F. J., Benjamin R. A., Heroux A. J., Langston G. I., 2008, *ApJ*, **679**, L21
- Martin P. G., 1988, *ApJS*, **66**, 125
- McKee C. F., 1989, *ApJ*, **345**, 782
- Munch G., 1952, *PASP*, **64**, 312
- Münch G., Zirin H., 1961, *ApJ*, **133**, 11
- Okamoto R., Yamamoto H., Tachihara K., Hayakawa T., Hayashi K., Fukui Y., 2017, *ApJ*, **838**, 132
- Oort J. H., 1966, *Bull. Astron. Inst. Netherlands*, **18**, 421
- Pagel B. E. J., Patchett B. E., 1975, *MNRAS*, **172**, 13
- Peterson J. D., Webber W. R., 2002, *ApJ*, **575**, 217
- Planck Collaboration XI 2014, *A&A*, **571**, A11
- Planck Collaboration X 2016, *A&A*, **594**, A10
- Planck Collaboration Int. XLVIII 2016, *A&A*, **596**, A109
- Reynolds R. J., 1991, in Bloemen H., ed., *The International Astronomical Union (IAU) Symposium Series Vol. 144, The Interstellar Disk-Halo Connection in Galaxies*. p. 67
- Richter P., Savage B. D., Wakker B. P., Sembach K. R., Kalberla P. M. W., 2001a, *ApJ*, **549**, 281
- Richter P., Sembach K. R., Wakker B. P., Savage B. D., Tripp T. M., Murphy E. M., Kalberla P. M. W., Jenkins E. B., 2001b, *ApJ*, **559**, 318
- Richter P., de Boer K. S., Werner K., Rauch T., 2015, *A&A*, **584**, L6
- Rocha-Pinto H. J., Maciel W. J., 1996, *MNRAS*, **279**, 447
- Roy A., et al., 2013, *ApJ*, **763**, 55
- Schwarz U. J., Wakker B. P., van Woerden H., 1995, *A&A*, **302**, 364
- Sembach K. R., et al., 2003, *ApJS*, **146**, 165
- Sembach K. R., et al., 2004, *ApJS*, **150**, 387
- Shapiro P. R., Field G. B., 1976, *ApJ*, **205**, 762
- Shelton R. L., Williams M. E., Parker M. C., Galyardt J. E., Fukui Y., Tachihara K., 2022, *ApJ*, **925**, 190
- Shull J. M., Jones J. R., Danforth C. W., Collins J. A., 2009, *ApJ*, **699**, 754
- Smoker J. V., Fox A. J., Keenan F. P., 2011, *MNRAS*, **415**, 1105
- Takahira K., Tasker E. J., Habe A., 2014, *ApJ*, **792**, 63
- Thom C., Putman M. E., Gibson B. K., Christlieb N., Flynn C., Beers T. C., Wilhelm R., Lee Y. S., 2006, *ApJ*, **638**, L97
- Thom C., Peek J. E. G., Putman M. E., Heiles C., Peek K. M. G., Wilhelm R., 2008, *ApJ*, **684**, 364
- Tripp T. M., et al., 2003, *AJ*, **125**, 3122
- Tsuge K., et al., 2019, *ApJ*, **871**, 44
- Tufte S. L., Reynolds R. J., Haffner L. M., 1998, *ApJ*, **504**, 773
- Wakker B. P., 2001, *ApJS*, **136**, 463
- Wakker B. P., et al., 1999, *Nature*, **402**, 388
- Wakker B. P., et al., 2007, *ApJ*, **670**, L113
- Wakker B. P., York D. G., Wilhelm R., Barentine J. C., Richter P., Beers T. C., Ivezić Ž., Howk J. C., 2008, *ApJ*, **672**, 298
- Wang J., Koribalski B. S., Serra P., van der Hulst T., Roychowdhury S., Kamphuis P., Chengalur J. N., 2016, *MNRAS*, **460**, 2143
- Weiß A., Heithausen A., Herbstmeier U., Mebold U., 1999, *A&A*, **344**, 955
- Wesselius P. R., Fejes I., 1973, *A&A*, **24**, 15
- Winkel B., Kerp J., Flöer L., Kalberla P. M. W., Ben Bekhti N., Keller R., Lenz D., 2016, *A&A*, **585**, A41

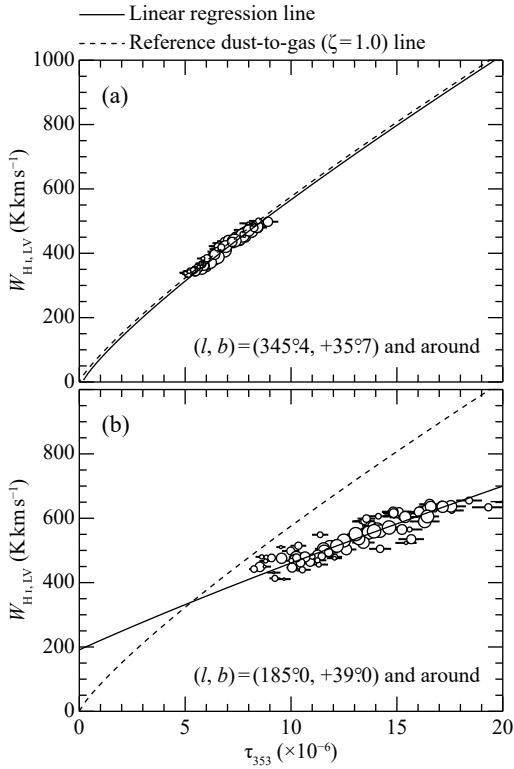


Figure A1. (a) Scatter plot showing the τ_{353} - $W_{\text{H I, LV}}$ correlation for data points within 1.2 deg of $(l, b) = (345^\circ 4, +35^\circ 7)$ where the LV H I emission is judged to be optically thin (not saturated). The solid lines show local regression lines described by equation (A1) at the position. The circle size represents the weight in the local regression which decays with the angular distance in the sky from the regression point (equation (10)). The horizontal bars show $\sigma(\tau_{353})$ (Planck Collaboration Int. XLVIII 2016). The dashed line indicates the reference dust-to-gas ratio ($\zeta = 1.0$). (b) Same as (a) but for data points within 1.2 deg of $(l, b) = (185^\circ 0, -39^\circ 0)$ where the LV H I emission is judged to be saturated. In both samples, the H I integrated intensity of the NHV, NIV, PIV, and PHV components are small enough ($W_{\text{H I, X}} < 5.5 \text{ K km s}^{-1}$ or $N_{\text{H I, X}}^* < 1 \times 10^{19} \text{ cm}^{-2}$), and their contribution to τ_{353} is approximately zero.

- Woolf V. M., West A. A., 2012, *MNRAS*, **422**, 1489
 van Woerden H., Wakker B. P., 2004, Distances and Metallicities of HVCS. p. 195, doi:10.1007/1-4020-2579-3_10
 van Woerden H., Schwarz U. J., Peletier R. F., Wakker B. P., Kalberla P. M. W., 1999, *Nature*, **400**, 138
 van den Bergh S., 1962, *AJ*, **67**, 486

APPENDIX A: MASKING

We masked the data points which meet any of the following criteria;

- Galactic latitude is $|b| < 15^\circ$ in order to eliminate contamination by the Galactic-disk components far from us.
- The CO integrated-intensity $W_{\text{CO}} > 1.4 \text{ K km s}^{-1}$ (corresponding to the 3σ level in $|b| > 15^\circ$), where the molecular gas is not negligible compared to the atomic gas.
- The areas covering nearby galaxies listed in either or both the catalog by Karachentsev et al. (2013) and the samples studied by Wang et al. (2016).
- H I emission is saturated due to the optical depth effect for

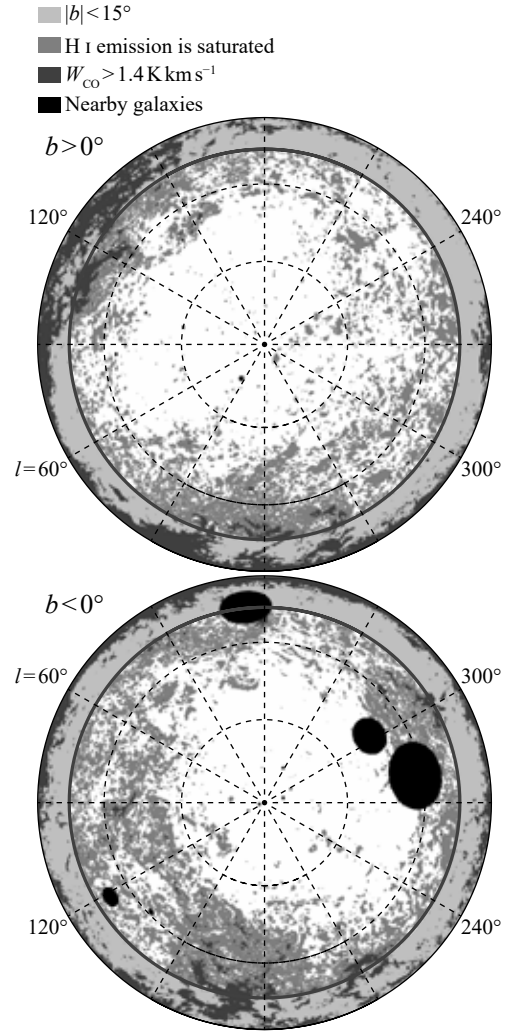


Figure A2. The masked areas in the present study shown in the same projection as Fig. 1. The low latitude zone $|b| < 15^\circ$ are delimited by thick solid lines. The dark-gray shadow outlines the data points with $W_{\text{CO}} > 1.4 \text{ K km s}^{-1}$ (Planck Collaboration X 2016). The black filled ellipses cover nearby galaxies taken from the catalog by Karachentsev et al. (2013) and samples studied by Wang et al. (2016). The light-gray shadow in $|b| > 15^\circ$ presents the areas where local H I emission is saturated.

lower spin temperature, in which case the $\tau_{353} \propto N_{\text{H I}}^\alpha$ relationship described in Section 4.1 is not applicable.

We employed a simple procedure to determine if each data point met the criterion (d); (1) redefined equation (9) adding a constant term τ_0 ,

$$\tau_{353}(l_i, b_i) = \left(\frac{C_0}{C}\right)^\alpha \sum_X [\zeta_X(l_i, b_i) W_{\text{H I, X}}(l_i, b_i)]^\alpha + \tau_0(l_i, b_i), \quad (\text{A1})$$

and estimate local parameters at the data point as described in Section 4.2 and Appendix D, then (2) determined that H I emission is saturated if $\hat{\tau}_0 \neq 0$. We set the threshold to $|\hat{\tau}_0| = 1 \times 10^{-6}$, the 1σ of all data points excluding (a) – (c). Fig. A1 shows the τ_{353} - $W_{\text{H I, LV}}$ correlations for optically thin (not saturated) and saturated examples. In both samples, the H I integrated intensity of the NHV, NIV, PIV,

and PHV components are small enough, and their contribution to τ_{353} is approximately zero. Fig. A2 summarizes the masked areas.

APPENDIX B: H α INTENSITY-TO-WIM COLUMN DENSITY CONVERSION FACTOR

A simple approach to converting $I_{H\alpha}$ to N_{H^+} is the following.

(1) $I_{H\alpha}$ is proportional to the rate of the recombination $2.584 \times 10^{-13} (T_e/10^4 \text{ K})^{-0.806} \text{ cm}^3 \text{ s}^{-1}$ and the mean number of H α photons produced per recombination $0.46 \times (T_e/10^4 \text{ K})^{-0.118}$ (Martin 1988),

$$\frac{I_{H\alpha}}{R} = \frac{1}{2.75} \int \left(\frac{T_e}{10^4 \text{ K}} \right)^{-0.924} \frac{n_e}{\text{cm}^{-3}} \frac{n_{H^+}}{\text{cm}^{-3}} \frac{1}{\text{pc}} dl, \quad (\text{B1})$$

where T_e is the electron temperature, n_e and n_{H^+} are the densities of electron and ionized hydrogen ($n_e \approx n_{H^+}$), and dl is the line-of-sight path length over which the electrons are recombining.

(2) The distribution of T_e and $n_e \approx n_{H^+}$ in a line of sight is usually unknown. We approximate that they are constant over the emitting region, and the path length of the ionized gas is given by

$$\frac{L}{\text{pc}} = 2.75 \left(\frac{T_e}{10^4 \text{ K}} \right)^{0.924} \left(\frac{\langle n_e \rangle}{\text{cm}^{-3}} \right)^{-2} \frac{I_{H\alpha}}{R}, \quad (\text{B2})$$

where $\langle n_e \rangle$ is the mean electron density in the line of sight. Then, N_{H^+} is given by

$$\begin{aligned} \frac{N_{H^+}}{\text{cm}^{-2}} &= 3.086 \times 10^{18} \frac{\langle n_{H^+} \rangle}{\text{cm}^{-3}} \frac{L}{\text{pc}} \\ &\approx 3.086 \times 10^{18} \times 2.75 \\ &\quad \times \left(\frac{T_e}{10^4 \text{ K}} \right)^{0.924} \left(\frac{\langle n_e \rangle}{\text{cm}^{-3}} \right)^{-1} \frac{I_{H\alpha}}{R}. \end{aligned} \quad (\text{B3})$$

(3) Previous works estimated that the thick disk WIM has a mid-plane volume-averaged electron density of $\sim 0.01 - 0.03 \text{ cm}^{-3}$ and a scale height of $\sim 1 - 2 \text{ kpc}$ (e.g., Gómez et al. 2001; Peterson & Webber 2002; Berkhuijsen & Müller 2008; Gaensler et al. 2008). Using $\langle n_e \rangle = 0.02 \text{ cm}^{-3}$ and $T_e = 8 \times 10^3 \text{ K}$, we obtain a conversion factor of

$$\frac{N_{H^+}}{\text{cm}^{-2}} = 3 \times 10^{20} \times \frac{I_{H\alpha}}{R}. \quad (\text{B4})$$

APPENDIX C: PLANCK PR2 DUST DATA VERSUS PR1 DUST DATA

We checked the consistency between *Planck* PR2 GNILC dust data (released version R2.01, Planck Collaboration Int. XLVIII 2016) and PR1 data (R1.20, Planck Collaboration XI 2014). Here, we did not smooth the R2.01 data but smoothed the R1.20 data to have the same effective beam size as the original R2.01 data. Then both were degraded to $N_{\text{side}} = 256$. Here, we applied the masking criteria (a) – (c) in Appendix A.

Fig. C1 shows the τ_{353} - τ_{353} correlation between R2.01 and R1.20. The two datasets are highly correlated with a correlation coefficient of 0.999 and a linear regression by an OLS-bisector method (Isobe et al. 1990) is

$$\tau_{353}(\text{R1.20}) = (1.0302 \pm 0.0003) \times \tau_{353}(\text{R2.01}) - (8.85 \pm 0.09) \times 10^{-8}. \quad (\text{C1})$$

We found a good consistency between $\tau_{353}(\text{R2.01})$ and $\tau_{353}(\text{R1.20})$.

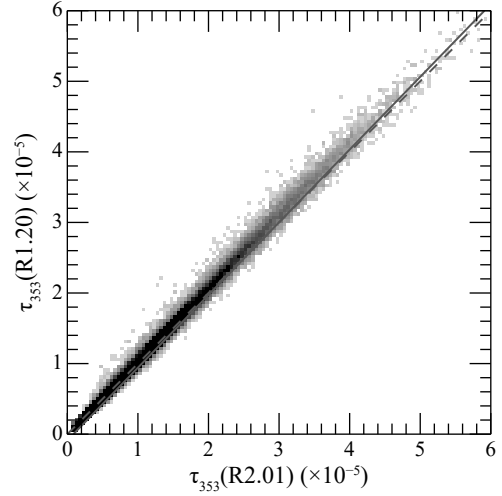


Figure C1. Density plot showing a correlation between $\tau_{353}(\text{R2.01})$ (Planck Collaboration Int. XLVIII 2016) and $\tau_{353}(\text{R1.20})$ (Planck Collaboration XI 2014). The solid line shows the linear regression line (equation (C1)) and the dashed line shows $\tau_{353}(\text{R1.20}) = \tau_{353}(\text{R2.01})$.

APPENDIX D: GEOGRAPHICALLY WEIGHTED REGRESSION ANALYSIS

D1 Estimating the Local Coefficients

Prior to the analysis, we performed a linearizing transformation on $W_{H1,k}$ ($k = 1, \dots, m$; $m = 5$ in the present study and corresponding to the five velocity ranges in Table 1)

$$x_k(l_i, b_i) = \begin{cases} [W_{H1,k}(l_i, b_i)]^\alpha & \text{if } W_{H1,k}(l_i, b_i) > 5.5 \text{ K km s}^{-1} \\ 0 & \text{otherwise} \end{cases} \quad (\text{D1})$$

and replaced other variables,

$$y(l_i, b_i) = \left(\frac{C}{C_0} \right)^\alpha \tau_{353}(l_i, b_i) \quad (\text{D2})$$

$$\beta_k(l_i, b_i) = [\zeta_k(l_i, b_i)]^\alpha \quad (\text{D3})$$

$$a(l_i, b_i) = \left(\frac{C}{C_0} \right)^\alpha \tau_0(l_i, b_i). \quad (\text{D4})$$

Equation (A1) was rewritten in a standard GWR form,

$$y(l_i, b_i) = \sum_{k=1}^m [\beta_k(l_i, b_i) x_k(l_i, b_i)] + a(l_i, b_i) + \varepsilon(l_i, b_i), \quad (\text{D5})$$

where $\varepsilon(l_i, b_i)$ is the error term. Equation (D5) can be rewritten in a matrix form

$$\mathbf{y} = (\mathbf{B} \circ \mathbf{X}) \mathbf{1}_{m \times n} + \mathbf{a} + \boldsymbol{\varepsilon}, \quad (\text{D6})$$

where \circ denotes the Hadamard product (also known as element-wise product) of the matrices,

$$\mathbf{X} = \begin{bmatrix} x_1(l_1, b_1) & \cdots & x_m(l_1, b_1) \\ \vdots & \ddots & \vdots \\ x_1(l_n, b_n) & \cdots & x_m(l_n, b_n) \end{bmatrix}, \quad (\text{D7})$$

is the matrix of the n observations of m independent variables,

$$\mathbf{B} = \begin{bmatrix} \beta_1(l_1, b_1) & \cdots & \beta_m(l_1, b_1) \\ \vdots & \ddots & \vdots \\ \beta_1(l_n, b_n) & \cdots & \beta_m(l_n, b_n) \end{bmatrix} = \begin{bmatrix} \boldsymbol{\beta}(l_1, b_1)^T \\ \vdots \\ \boldsymbol{\beta}(l_n, b_n)^T \end{bmatrix} \quad (\text{D8})$$

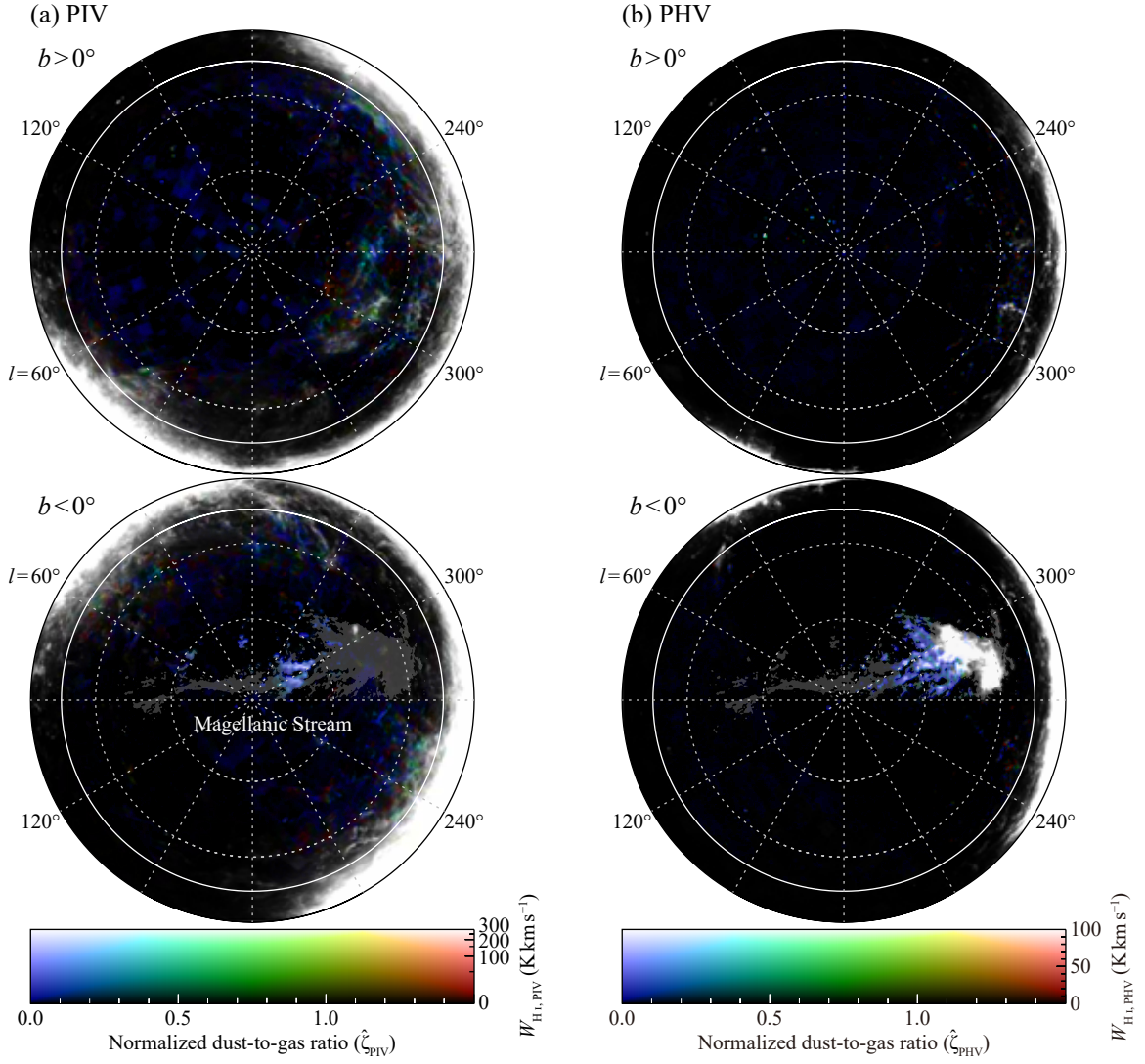


Figure D1. Same as Fig. 7 but for (a) PIV and (b) PHV.

is n set of local coefficients, and $\mathbf{1}_{m \times n}$ is an $m \times n$ all-ones matrix. The n -element vectors \mathbf{y} , \mathbf{a} , and $\boldsymbol{\varepsilon}$ are dependent variables, local constant terms, and error terms.

The local regression coefficients at the i -th regression point is given by solving

$$\hat{\boldsymbol{\beta}}_i = (\mathbf{X}_i^T \mathbf{W}_i \mathbf{X}_i)^{-1} \mathbf{X}_i^T \mathbf{W}_i \mathbf{y}_i, \quad (\text{D9})$$

where

$$\mathbf{X}_i = (\mathbf{I}_n - \mathbf{W}_i \mathbf{1}_{n \times n}) \mathbf{X} \quad (\text{D10})$$

is the local-centered independent variables,

$$\mathbf{y}_i = (\mathbf{I}_n - \mathbf{W}_i \mathbf{1}_{n \times n}) \mathbf{y}, \quad (\text{D11})$$

is the local-centered dependent variable, \mathbf{I}_n is the identity matrix of size n , $\mathbf{1}_{n \times n}$ is an $n \times n$ all-ones matrix, $\boldsymbol{\beta}_i$ is a short-hand notation for $\boldsymbol{\beta}(l_i, b_i)$, the superscript T indicates the matrix transpose, \mathbf{W}_i is a weighting matrix

$$\mathbf{W}_i = \frac{1}{\sum_{j=1}^n w_i(l_j, b_j)} \begin{bmatrix} w_i(l_1, b_1) & & & \\ & \ddots & & \\ & & \ddots & \\ & & & w_i(l_n, b_n) \end{bmatrix}, \quad (\text{D12})$$

and $w_i(l_j, b_j)$ is given by equation (10). As each component of $\boldsymbol{\beta}_i$ should be non-negative ($\boldsymbol{\beta}_i \geq 0$), equation (D9), therefore, must be reformulated by a non-negative least-squares (NNLS) problem

$$\text{Minimize } \|\mathbf{W}_i (\mathbf{X}_i \boldsymbol{\beta}_i - \mathbf{y}_i)\| \text{ subject to } \boldsymbol{\beta}_i \geq 0, \quad (\text{D13})$$

where $\|\cdot\|$ denotes Euclidean norm (or also called L^2 norm). A widely used algorithm for solving NNLS problems is the one by Lawson & Hanson (1995) briefly summarized as follows.

1. Initialize set $P = \emptyset$ and $Q = \{1, \dots, m\}$.
2. Let $\mathbf{u} = (u_1 \ \dots \ u_m) = \mathbf{X}_i^T (\mathbf{y}_i - \mathbf{X}_i \boldsymbol{\beta}_i)$.
3. If $Q = \emptyset$ or $\max\{u_q : q \in Q\} \leq 0$, the calculation is completed.
4. Find an index $k \in Q$ such that $u_k = \max\{u_q : q \in Q\}$, and then move the index k from Q to P .
5. Let \mathbf{P}_i denote the $n \times m$ matrix defined by

$$\text{column } k \text{ of } \mathbf{P}_i = \begin{cases} \text{column } k \text{ of } \mathbf{X}_i & \text{if } k \in P \\ 0 & \text{if } k \in Q. \end{cases} \quad (\text{D14})$$

6. Let \mathbf{z} be vector of same length as $\boldsymbol{\beta}_i$, and set

$$\mathbf{z} = (z_1 \ \dots \ z_m) = (\mathbf{P}_i^T \mathbf{P}_i)^{-1} \mathbf{P}_i^T \mathbf{y}_i. \quad (\text{D15})$$

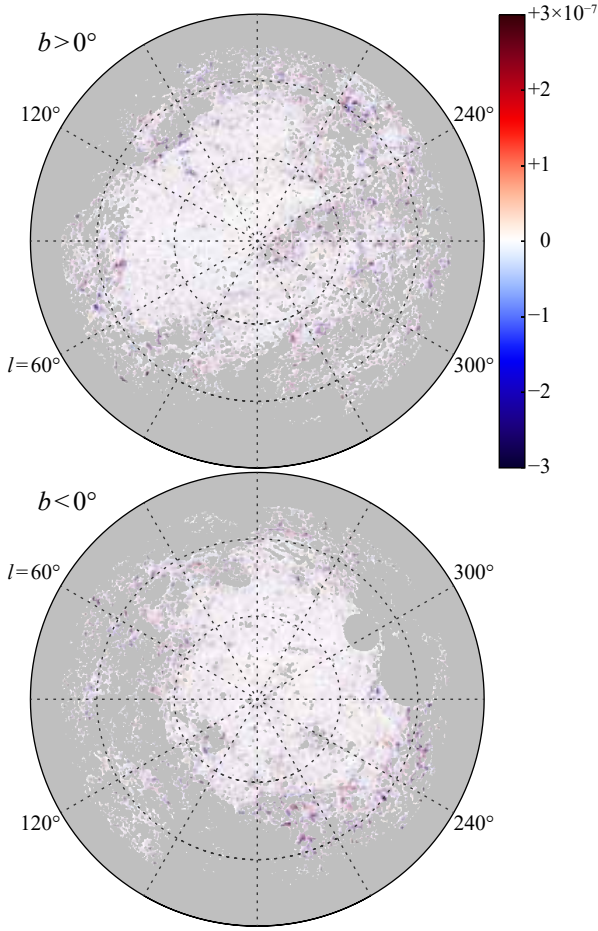


Figure D2. Residuals from the regression.

7. Set $z_q = 0$ for $q \in Q$.
8. If $\min\{z_p : p \in P\} > 0$, set $\beta_i = z$ and go to Step 2.
9. Let

$$\gamma = \min \left\{ \frac{\beta_p}{\beta_p - z_p} : z_p \leq 0, p \in P \right\}, \quad (\text{D16})$$

where β_p means the p -th element of β_i .

10. Set β_i to $\beta_i + \gamma(z - \beta_i)$.

11. Move from P to Q all indices $p \in P$ such that $\beta_p \leq 0$. Then go to Step 5.

The obtained β_i satisfies $\beta_p > 0$ for $p \in P$, $\beta_q = 0$ for $q \in Q$, and is an estimator $\hat{\beta}_i$ for the least squares problem

$$\mathbf{P}_i \beta_i = y_i. \quad (\text{D17})$$

The estimator of the constant term is given by

$$\hat{a}(l_i, b_i) = \mathbf{1}_{1 \times n} \mathbf{W}_i \left[y - \mathbf{X} \hat{\beta}_i \right], \quad (\text{D18})$$

where $\mathbf{1}_{1 \times n}$ is an n -element all-ones row vector.

The estimated regression coefficients are transformed as following

$$\hat{\zeta}_k(l_i, b_i) = \left[\hat{\beta}_k(l_i, b_i) \right]^{1/\alpha} \quad (\text{D19})$$

$$\hat{\tau}_0(l_i, b_i) = \left(\frac{C_0}{C} \right)^\alpha \hat{a}(l_i, b_i). \quad (\text{D20})$$

Figs. 7 and D1 show $\hat{\zeta}_k(l_i, b_i)$. Fig. D2 shows the residuals from

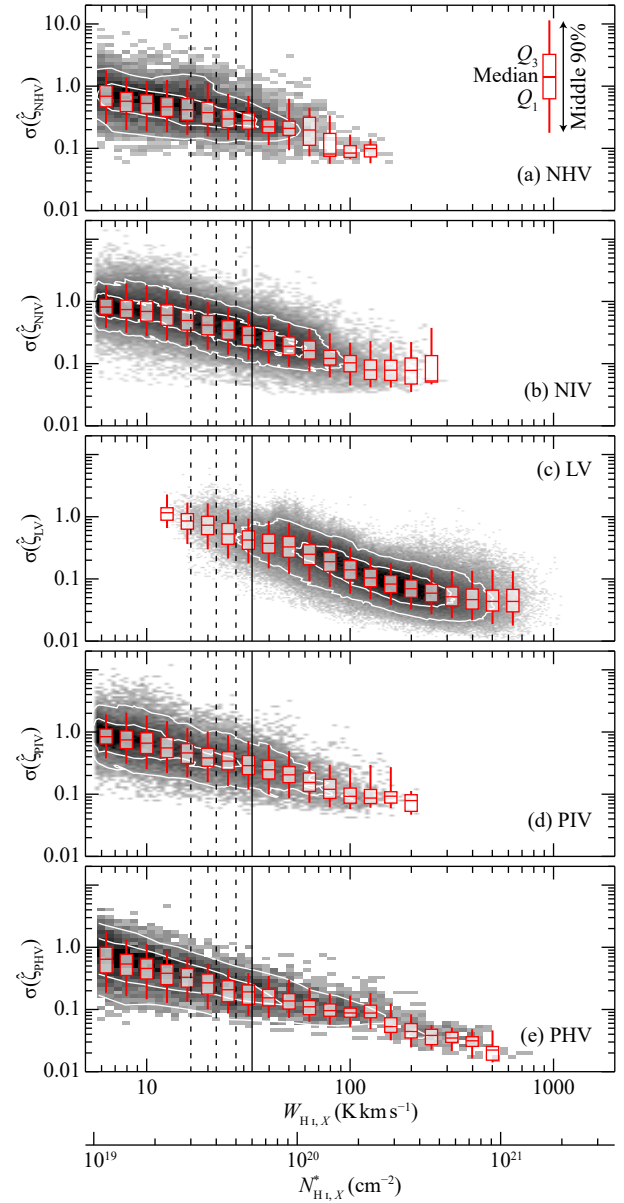


Figure D3. Density plot showing correlation between $\sigma(\hat{\zeta}_X)$ and $W_{\text{H1},X}$ in (a) NHV, (b) NIV, (c) LV, (d) PIV, and (e) PHV. The vertical lines indicate $W_{\text{H1},X} = 16, 22, 27, \text{ and } 33 \text{ K km s}^{-1}$ (corresponding to $N_{\text{H1},X}^* = 3, 4, 5, \text{ and } 6 \times 10^{19} \text{ cm}^{-2}$). The contours contain 50 and 90 per cent of data points. The overlaid box-and-whisker plot presents the median (the horizontal bar), the first and third quartiles (Q_1 and Q_3 , the lower and upper ends of the box), and the 5th and 95th percentiles (the lower and upper ends of the whisker) in each bin.

the regression given by $\tau_{353}(l_i, b_i) - \hat{\tau}_{353}(l_i, b_i)$. The median and interquartile range of the residuals are -1.5×10^{-9} and 5.9×10^{-8} , respectively.

D2 The Standard Error of the Estimated Local Coefficients

Let

$$\mathbf{C}_i = \left(\mathbf{P}_i^T \mathbf{W}_i \mathbf{P}_i \right)^{-1} \mathbf{P}_i^T \mathbf{W}_i, \quad (\text{D21})$$

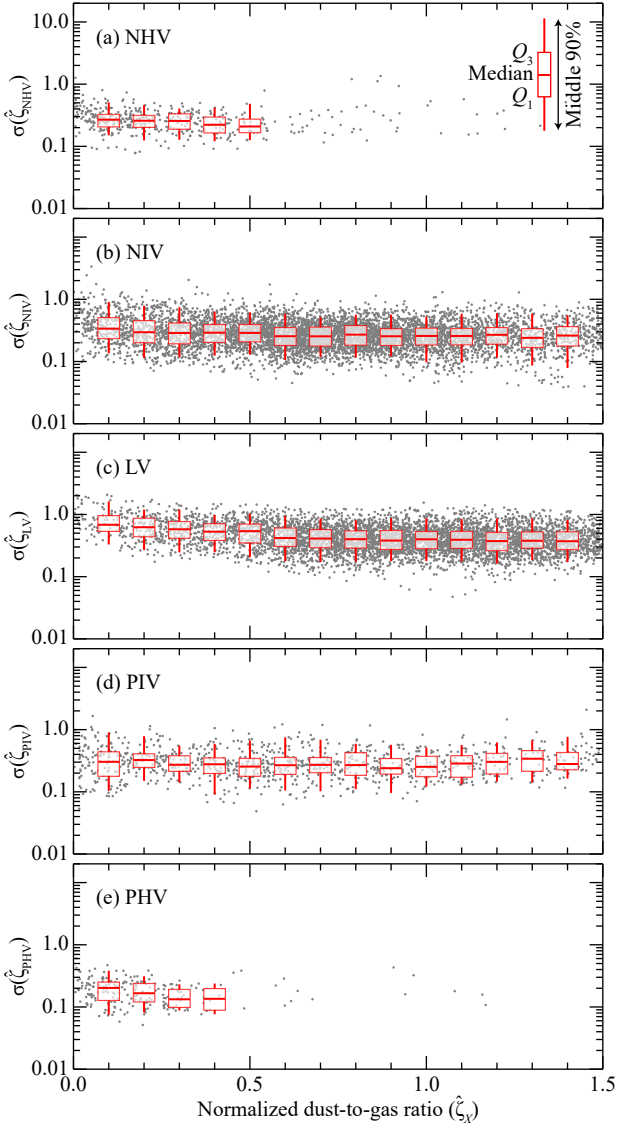


Figure D4. Scatter plot showing $\sigma(\widehat{\zeta}_X)$ with respect to $\widehat{\zeta}_X$ for the data points with $N_{\text{H I}, X} = 5.5 - 6.5 \times 10^{19} \text{ cm}^{-2}$ in (a) NHV, (b) NIV, (c) LV, (d) PIV, and (e) PHV. The overlaid box-and-whisker plot presents the median, Q_1 , Q_3 , and the 5th/95th percentiles in each bin, similarly as in Figure D3.

where \mathbf{P}_i satisfies

$$\text{column } k \text{ of } \mathbf{P}_i = \begin{cases} \text{column } k \text{ of } \mathbf{X}_i & \text{if the } k\text{-th element of } \widehat{\beta}_i > 0 \\ 0 & \text{if the } k\text{-th element of } \widehat{\beta}_i = 0 \end{cases} \quad (\text{D22})$$

Then the estimated variance-covariance matrix of $\widehat{\beta}(l_i, b_i)$ is denoted by

$$\Sigma_i = \sigma^2 \mathbf{C}_i \mathbf{C}_i^T, \quad (\text{D23})$$

where σ^2 is the normalized residual sum of squares (RSS) from the local regression

$$\sigma^2 = \frac{\|\mathbf{y} - \widehat{\mathbf{y}}\|^2}{n - 2\text{tr}\mathbf{S} + \text{tr}(\mathbf{S}^T \mathbf{S})} \sim \frac{\|\mathbf{y} - \widehat{\mathbf{y}}\|^2}{n - \text{tr}\mathbf{S}}. \quad (\text{D24})$$

The vector of predicted values $\widehat{\mathbf{y}}$ is given by

$$\begin{aligned} \widehat{\mathbf{y}} &= (\widehat{\mathbf{B}} \circ \mathbf{X}) \mathbf{1}_{m \times n} + \widehat{\mathbf{a}} \\ &= \left\{ \begin{bmatrix} \widehat{\beta}(l_1, b_1)^T \\ \vdots \\ \widehat{\beta}(l_n, b_n)^T \end{bmatrix} \circ \mathbf{X} \right\} \mathbf{1}_{m \times n} + \begin{bmatrix} \widehat{a}(l_1, b_1) \\ \vdots \\ \widehat{a}(l_n, b_n) \end{bmatrix}. \end{aligned} \quad (\text{D25})$$

The matrix \mathbf{S} is the hat matrix which maps $\widehat{\mathbf{y}}$ on to \mathbf{y}

$$\widehat{\mathbf{y}} = \mathbf{S} \mathbf{y}, \quad (\text{D26})$$

and the i -th row of \mathbf{S} is given by

$$\mathbf{s}_i = (\text{row } i \text{ of } \mathbf{X}_i) \mathbf{C}_i (\mathbf{I}_n - \mathbf{W}_i \mathbf{1}_{n \times n}) + \mathbf{1}_{1 \times n} \mathbf{W}_i. \quad (\text{D27})$$

The standard errors of the components of $\widehat{\beta}(l_i, b_i)$, $\sigma[\widehat{\beta}_k(l_i, b_i)]$ are obtained from square roots of diagonal elements of Σ_i . The estimated standard errors are transformed as

$$\sigma(\widehat{\zeta}_k)(l_i, b_i) = \frac{1}{\alpha} \widehat{\beta}_k [\widehat{\beta}_k(l_i, b_i)]^{1/\alpha - 1} \sigma[\widehat{\beta}_k(l_i, b_i)]. \quad (\text{D28})$$

Figs. D3 and D4 show that $\sigma(\widehat{\zeta}_X)$ is inversely proportional to $W_{\text{H I}, X}$ (or $N_{\text{H I}, X}^*$), but is not dependent on $\widehat{\zeta}_X$.

This paper has been typeset from a $\text{\TeX}/\text{\LaTeX}$ file prepared by the author.